



## King's Research Portal

DOI:

[10.1016/j.devcel.2023.02.011](https://doi.org/10.1016/j.devcel.2023.02.011)

*Document Version*

Peer reviewed version

[Link to publication record in King's Research Portal](#)

*Citation for published version (APA):*

Chen, H.-J., Barske, L., Talbot, J. C., Dinwoodie, O., Roberts, R., Farmer, DJ., Jimenez, C., Merrill, A. E., Tucker, A. S., & Crump, J. G. (2023). Nuclear Receptor Nr5a2 Promotes Diverse Connective Tissue Fates in the Jaw. *Developmental Cell*, 58(6), 461-473.e7. <https://doi.org/10.1016/j.devcel.2023.02.011>

### **Citing this paper**

Please note that where the full-text provided on King's Research Portal is the Author Accepted Manuscript or Post-Print version this may differ from the final Published version. If citing, it is advised that you check and use the publisher's definitive version for pagination, volume/issue, and date of publication details. And where the final published version is provided on the Research Portal, if citing you are again advised to check the publisher's website for any subsequent corrections.

### **General rights**

Copyright and moral rights for the publications made accessible in the Research Portal are retained by the authors and/or other copyright owners and it is a condition of accessing publications that users recognize and abide by the legal requirements associated with these rights.

- Users may download and print one copy of any publication from the Research Portal for the purpose of private study or research.
- You may not further distribute the material or use it for any profit-making activity or commercial gain
- You may freely distribute the URL identifying the publication in the Research Portal

### **Take down policy**

If you believe that this document breaches copyright please contact [librarypure@kcl.ac.uk](mailto:librarypure@kcl.ac.uk) providing details, and we will remove access to the work immediately and investigate your claim.

## Nuclear Receptor Nr5a2 Promotes Diverse Connective Tissue Fates in the Jaw

Hung-Jhen Chen<sup>1</sup>, Lindsey Barske<sup>1,2</sup>, Jared C. Talbot<sup>3</sup>, Olivia M. Dinwoodie<sup>4</sup>, Ryan R. Roberts<sup>1,5</sup>, D'Juan T. Farmer<sup>1,6</sup>, Christian Jimenez<sup>1</sup>, Amy E. Merrill<sup>5</sup>, Abigail S. Tucker<sup>4</sup> and J. Gage Crump<sup>1,\*</sup>

<sup>1</sup>Eli and Edythe Broad Center for Regenerative Medicine, Department of Stem Cell Biology and Regenerative Medicine, Keck School of Medicine, University of Southern California, Los Angeles, CA 90033, USA.

<sup>2</sup>Division of Human Genetics, Cincinnati Children's Hospital Medical Center, Cincinnati, OH 45229, USA; Department of Pediatrics, University of Cincinnati College of Medicine, Cincinnati, OH 45229, USA.

<sup>3</sup>School of Biology and Ecology, University of Maine, Orono, ME 04469, USA.

<sup>4</sup>Centre for Craniofacial and Regenerative Biology, King's College London, London, UK.

<sup>5</sup>Department of Biomedical Sciences, Center for Craniofacial Molecular Biology, Ostrow School of Dentistry, University of Southern California, Los Angeles, CA 90033, USA; Department of Biochemistry and Molecular Medicine, Keck School of Medicine, University of Southern California, Los Angeles, CA 90033, USA.

<sup>6</sup>Molecular, Cell and Developmental Biology Department and Orthopaedic Surgery, University of California, Los Angeles, CA 90095, USA.

\* Lead Contact: J. Gage Crump, [gcrump@usc.edu](mailto:gcrump@usc.edu), (323) 442-2693

## Summary

Organ development involves sustained production of diverse cell types with spatiotemporal precision. In the vertebrate jaw, neural-crest-derived progenitors produce not only skeletal tissues but also later-forming tendons and salivary glands. Here we identify the pluripotency factor Nr5a2 as essential for cell fate decisions in the jaw. In zebrafish and mice, we observe transient expression of Nr5a2 in a subset of mandibular post-migratory neural-crest-derived cells. In zebrafish *nr5a2* mutants, *nr5a2*-expressing cells that would normally form tendons generate excess jaw cartilage. In mice, neural crest-specific *Nr5a2* loss results in analogous skeletal and tendon defects in the jaw and middle ear, as well as salivary gland loss. Single-cell profiling identifies that Nr5a2, distinct from its roles in pluripotency, promotes jaw-specific chromatin accessibility and gene expression essential for tendon and gland fates. Thus, repurposing of Nr5a2 promotes connective tissue fates to generate the full repertoire of derivatives required for jaw and middle ear function.

## Introduction

The gnathostome jaw is a remarkable evolutionary innovation that facilitated predation, feeding, and communication. In addition to the jaw skeleton (bone, cartilage, and teeth), multiple soft connective tissue components are required for its function. For example, tendons connect the jaw skeleton to musculature, ligaments stabilize the jaw joint, and salivary glands lubricate the oral cavity. Remarkably, the jaw skeleton, tendons, ligaments, and salivary gland mesenchyme all arise from cranial neural crest-derived cells (CNCCs) of the mandibular arch<sup>1-5</sup>. CNCCs closer to the future oral cavity gives rise to Meckel's cartilage, intramembranous regions of the dentary bone, and teeth, while CNCCs located in the more posterior (i.e. aboral) domain of the mandibular arch contribute to jaw tendons and salivary gland mesenchyme. In mammals, the more proximal domains of the mandibular arch also give rise to skeletal and connective tissue elements of the middle ear<sup>6</sup>. The mechanisms that induce skeletal versus non-skeletal connective tissue fates from mandibular arch CNCCs remain unclear.

Transcription factors for skeletal and connective tissue fates in the jaw and middle ear, as well as the rest of the body, have been identified. Sox9 and Runx2 are essential for the specification of cartilage<sup>7,8</sup> and bone<sup>9</sup>, respectively, and Scleraxis (Scx) is important for tendon and ligament formation<sup>10,11</sup>. Sox9 is also regionally activated in distal mandibular epithelium, in part by a local mesenchymal source of Fgf10, to induce salivary gland development<sup>12</sup>. However, we have an incomplete understanding of how the expression of lineage-specific transcription factors, such as Sox9 and Scx, is restricted to precise spatiotemporal mesenchymal domains. While the expression of these transcription factors is likely controlled by region-specific enhancers, the upstream factors controlling their region-specific expression have yet to be identified.

CNCCs contribute to a wide diversity of cell types<sup>13</sup>. It remains debated, however, if their multilineage capacity is endowed during specification or acquired after their migration into the head (reviewed in<sup>14</sup>). Whereas experiments in frog suggested that CNCCs might retain pluripotency from blastula stages<sup>15</sup>, later studies in mouse support a reacquisition of multipotency at CNCC specification stages due to induction of pluripotency factors Oct4 and Sox2<sup>16</sup>. Our recent single-cell genomic analysis of CNCC differentiation in zebrafish shows that the majority of enhancers required for CNCC lineage capacity gain accessibility after CNCCs migrate into the jaw-forming mandibular arch<sup>17</sup>. This suggests that opening of lineage-specific enhancers, and therefore access to transcription factors, plays a major role in determining the range of potential fates for CNCCs in the developing face, yet few factors that regulate CNCC enhancer accessibility have been identified.

Through single-cell profiling of zebrafish CNCCs, we recently identified *nr5a2* as a highly specific marker of the aboral domain of the mandibular arch of zebrafish<sup>17</sup>. Nr5a2 is a member of the nuclear receptor transcription factor family and is considered orphan as a physiological ligand remains unknown. Nr5a2 functions to maintain *Oct4* expression in mouse embryonic stem cells<sup>18</sup> and can replace Oct4 in reprogramming to induced pluripotent cells<sup>19</sup>. Reflective of this key role in pluripotency, loss of *Nr5a2* in mouse

results in lethality at blastula stages, around embryonic (E) day 6.5<sup>18,20</sup>. Nr5a2 also has roles in development of the liver<sup>20</sup>, pancreas<sup>21</sup>, and nervous system<sup>22</sup>. Whereas zebrafish *nr5a2* mutants have liver and pancreas defects, effects on CNCC differentiation and jaw development were not examined<sup>23</sup>. Here we found that Nr5a2 plays a conserved role in the aboral mandibular domain of zebrafish and mouse embryos where it promotes tendon and salivary gland fates at the expense of skeletal fates. In particular, we found that Nr5a2 establishes accessibility of enhancers required for maintaining undifferentiated progenitors while priming them for later tendon and gland differentiation. These targets of Nr5a2 in CNCCs are distinct from those described in embryonic stem cells<sup>19</sup>. Nr5a2 therefore promotes diverse connective tissue fates at the expense of skeletal fates in a restricted subset of postmigratory mandibular CNCCs through binding to genomic targets distinct from those important for pluripotency.

## Results

### Conserved expression of *Nr5a2* within the zebrafish and mouse mandibular arches

In single-cell transcriptome and chromatin accessibility analysis of zebrafish CNCCs, we previously identified *nr5a2* expression and the Nr5a2 DNA-binding motif as being highly enriched in the aboral domain of the mandibular arch (i.e. opposite to the oral epithelium) at 1.5 days post-fertilization (dpf)<sup>17</sup>. In situ hybridization for *nr5a2* mRNA identified highly specific expression in *dlx2a*+ mesenchyme of the mandibular arch at 1.5 dpf, posterior to the *sox9a*+ lower jaw Meckel's cartilage at 2 and 3 dpf (Fig. 1A-C). Previously published in situ patterns indicate a lack of CNCC expression at stages earlier than 1.5 dpf<sup>24</sup>, which agrees with bulk RNA sequencing studies of migratory CNCCs in zebrafish<sup>25</sup>. We also generated a *nr5a2:membrane-GFP* knock-in reporter line (*nr5a2*<sup>mGFP</sup>) by inserting membrane-GFP in the 5' untranslated region of the *nr5a2* locus via homologous recombination. Consistent with endogenous expression, *nr5a2*<sup>mGFP</sup> labeled the aboral mandibular domain at 2 and 3 dpf, with mesenchymal

*nr5a2<sup>mGFP</sup>* expression partially co-localizing with the tenocyte marker *scxa:mCherry* but not the cartilage maker *col2a1a:mCherry* (Fig. 1D; Fig. S1A; Fig. 2SA). We also observed weak *nr5a2:mGFP* expression in mesenchyme adjacent to cartilage in the neurocranium (Fig. S1B). Sequential live imaging of individuals identified that *nr5a2<sup>mGFP</sup>* expression precedes that of *scxa:mCherry*, with *nr5a2<sup>mGFP</sup>* being downregulated in *scxa:mCherry+* tenocytes as they mature (Fig. S1C). Thus, *nr5a2* expression is transiently upregulated in postmigratory mandibular CNCCs that are precursors for tendon but not cartilage cells.

We next examined whether mandibular expression of *Nr5a2* is conserved in mouse. Examination of mouse mandibular arch single-cell transcriptome data at E10.5<sup>26</sup> identified expression of *Nr5a2* in a putative aboral domain complementary to an oral domain marked by *Pitx1* expression (Fig. S1F), as in zebrafish<sup>17</sup>. In situ hybridization at E11.5 and E12.5 identified mesenchymal expression of *Nr5a2* at the posterior boundary of the mandibular arch and anterior boundary of the hyoid arch. As in zebrafish, mandibular *Nr5a2* expression was observed just posterior to developing *Sox9+* Meckel's cartilage in mouse (Fig. 1E, Fig. S1D,E). In more lateral regions, we observed *Nr5a2* expression between the first pharyngeal pouch and first pharyngeal cleft (Fig. S1D,E). At E14.5, *Nr5a2* expression was observed in mesenchyme of the palate and flanking the basisphenoid-forming region of the skull base, in mesenchyme surrounding the malleus, incus, and external auditory meatus, and in salivary gland mesenchyme (Fig. S1G)<sup>27</sup>, with single-cell transcriptome profiles of mouse submandibular glands<sup>28</sup> further confirming salivary gland mesenchyme expression that decreased from E12 to E16 (Fig. S1H). *Nr5a2* is therefore expressed in the mandibular arches of both fish and mammals, though it appears to be more prominently restricted to the aboral domain in fish.

### **Requirement for *nr5a2* in zebrafish lower jaw development**

Given the restricted mandibular expression of *nr5a2*, we investigated its requirement in zebrafish jaw development. We first examined homozygous *nr5a2<sup>oz3/oz3</sup>* mutant zebrafish, in which an early frameshift mutation results in premature truncation of the

protein before the DNA-binding and ligand-binding domains<sup>23</sup> (Fig. S2A). Mutant fish displayed an open mouth, and skeletal staining showed an enlarged Meckel's cartilage of the lower jaw, but no other craniofacial skeletal defects, at 6 and 10 dpf (Fig. 2A; Fig. S2B). Repeated live imaging identified increased numbers of *col2a1a:h2az2a-mCherry-2A-EGFP-CAAX*+ Meckel's chondrocytes in *nr5a2* mutants versus wild-type sibling controls from 2.5 dpf, the earliest stage at which labeled chondrocytes appear, through 7 dpf (Fig. 2B,C). The numbers of proliferating Meckel's chondrocytes, as assessed by anti-phospho-Histone-H3 staining, was unchanged at 2.5 and 3 dpf (Fig. S2C). Enlargement of Meckel's cartilage in mutants is therefore likely due to increased specification and not increased proliferative expansion of chondrocytes.

We next examined whether increased numbers of Meckel's chondrocytes are accompanied by concomitant loss of other CNCC derivatives. Meckel's cartilage is connected to lower jaw muscles by CNCC-derived *scxa:mCherry*+ tenocytes at 2.5 and 3 dpf, with these condensing at intermandibular tendons by 4 dpf (Fig. 1A, 2D). In *nr5a2* mutants, we observed variable disorganization and loss of *scxa:mCherry*+ lower jaw tenocytes, which was accompanied by disorganization of the lower jaw muscles (Fig. 2D,E; Fig. S2D). The interopercular–mandibular ligament, which stabilizes the jaw joint, was also missing in 12/13 mutants at 6 dpf, yet hyoid arch-derived tendons were largely unaffected (Fig. 2D, Fig. S2E). The lower-jaw-specific expansion of cartilage, loss of tendon and ligament, and disorganization of muscle precisely correlates with the highly localized expression of *nr5a2* in the aboral mandibular arch from which these structures derive.

### **Nr5a2 functions cell-autonomously in zebrafish CNCCs to specify tenocytes at the expense of chondrocytes**

To investigate the cellular basis of jaw tenocyte loss in *nr5a2* mutant zebrafish, we performed short-term lineage tracing with *nr5a2*<sup>mGFP</sup>. Homozygous *nr5a2*<sup>mGFP/mGFP</sup> fish displayed normal lower jaw cartilage and muscle and were adult viable; we did observe subtle jaw muscle defects in *nr5a2*<sup>mGFP/oz3</sup> but not *nr5a2*<sup>+/oz3</sup> fish, suggesting that the

*nr5a2*<sup>mGFP</sup> allele is a weak hypomorph (Fig. S2B,D). To create a severe loss-of-function allele in cis to the mGFP insertion, we injected CRISPR-Cas9 reagents into *nr5a2*<sup>mGFP</sup> fish and obtained progeny with an in-frame deletion of three amino acids (*nr5a2*<sup>mGFP-DBD-del</sup>) that removes a critical zinc finger motif-forming cysteine residue in the DNA-binding domain (Fig. S2A). We observed similar enlargement of Meckel's cartilage and muscle disorganization in *nr5a2*<sup>mGFP-DBD-del/mGFP-DBD-del</sup> and *nr5a2*<sup>oz3/oz3</sup> fish, indicating that disruption of the DNA-binding domain generates a severe loss-of-function allele (Fig. S2B,D). The similarity of cartilage defects in the *mGFP-DBD-del* and early frameshift *oz3* alleles also argues against genetic compensation, i.e. transcriptional adaptation in response to nonsense-mediated decay, in the *oz3* allele <sup>29</sup>.

In *nr5a2*<sup>mGFP-DBD-del/+</sup> controls, mGFP+ cells contributed to *scxa:mCherry*+ jaw tenocytes but only rarely to Meckel's chondrocytes at 3 dpf, which we confirmed by lack of co-expression of the cartilage marker *col2a1a:mCherry-NTR*+ at 2.5 dpf. In contrast in *nr5a2*<sup>mGFP-DBD-del/mGFP-DBD-del</sup> mutants, increased numbers of mGFP+ cells contributed to Meckel's cartilage and co-expressed *col2a1a:mCherry-NTR*, with a concomitant decrease in contribution to *scxa:mCherry*+ jaw tenocytes (Fig. 3A,B). These observations indicate that *nr5a2*-expressing cells shift from a tenocyte to chondrocyte fate in the absence of Nr5a2.

To further test the sufficiency of *nr5a2* in CNCCs for jaw patterning, we performed unilateral transplantation of wild-type BFP+ CNCC precursors into *nr5a2* mutants (Fig. 3C). In contrast to contralateral mutant sides, 4/4 sides with mandibular contribution of wild-type BFP+ CNCCs displayed rescue of Meckel's cartilage morphology based on *col2a1a:h2az2a-mCherry-2A-EGFP-CAAX* expression and Alcian Blue staining. We also observed rescue of lower jaw muscle organization in transplanted sides, with wild-type CNCCs forming cells with tenocyte morphology at the junction of muscle and cartilage. In two examples, wild-type CNCCs rescued Meckel's cartilage morphology without contributing to chondrocytes, indicating a non-cell-autonomous role of Nr5a2 in



patterning Meckel's cartilage (Fig. 3C; Fig. S3A). Thus, Nr5a2 functions to suppress chondrocyte differentiation in cells adjacent to the developing Meckel's cartilage.

### **Nr5a2 misexpression mildly suppresses chondrogenesis and disrupts tendon formation in the zebrafish lower jaw**

To test whether Nr5a2 is sufficient to repress lower jaw chondrogenesis, we generated a *UAS:nr5a2* transgenic line and crossed it to a CNCC mesenchyme-specific *fli1a:Gal4VP16* driver<sup>30</sup>, resulting in *nr5a2* expression throughout CNCC mesenchyme. Compared to single-positive *fli1:Gal4VP16* and *UAS:nr5a2* controls, Meckel's cartilage of *fli1a:Gal4VP16; UAS:nr5a2* fish had an abnormal pointed morphology and a 12-16% reduction in chondrocyte number, as assessed by *col2a1a:EGFP* and nuclear DAPI staining (Fig. S3B). Misexpression of *nr5a2* also resulted in ectopic *scxa:mCherry*<sup>+</sup> tenocytes and disorganized lower jaw muscle fibers, with occasional fibers connecting to ectopic tenocytes; the number of *scxa:mCherry*<sup>+</sup> tenocytes in the normal lower jaw attachment region, however, were unchanged (Fig. S3C). While tenocyte defects could reflect increased specification and/or disrupted migration and morphogenesis, our data show that Nr5a2 misexpression only mildly suppresses cartilage differentiation in the lower jaw.

### **Requirement for Nr5a2 in mouse NCCs for lower jaw and middle ear development**

We next examined whether *Nr5a2* has a similar requirement for development of mandibular arch-derived structures in mouse. As homozygous loss of *Nr5a2* results in lethality at epiblast stages<sup>20</sup>, we utilized the *Wnt1-Cre* driver and a *Nr5a2-flox* allele to delete both copies of *Nr5a2* in NCCs (*Nr5a2<sup>NCC</sup>*). *Nr5a2<sup>NCC</sup>* animals died shortly after birth due to unidentified causes, with air bubbles apparent in their intestines (Fig. S4A). Whereas overall head length was similar between newborn controls and *Nr5a2<sup>NCC</sup>* animals, staining for cartilage and bone identified abnormalities in skeletal structures derived from the mandibular arch (Fig. 4A; Fig. S4F). While Meckel's cartilage was largely unaffected at E14.5 (Fig. S4B), at birth the malleus cartilage, which derives from the proximal portion of Meckel's, was enlarged. We also observed shortening and

thickening of the angular process of the mandibular bone, as well as the tympanic ring and gonial bones of the middle ear (Fig. 4A; Fig. S4F). In the pterygoid plate of the cranial base, mutants displayed abnormal ossification at lateral edges and truncated medial bones (Fig. S4C) consistent with *Nr5a2* expression in this region at E14.5 (Fig. S1G).

We next used *Scx-GFP* to examine the effects of NCC-specific *Nr5a2* deletion on tendon development. In *Nr5a2<sup>NCC</sup>*; *Scx-GFP* newborn mice, the tendons connecting to the angular process of the lower jaw were reduced and dysmorphic. Histology identified dysmorphology of the connective tissue at the muscle insertion site, and detachment of muscle fibers that was confirmed by MF20 staining (Fig. 4B; Fig. S4D-F). The tensor tympani tendon connecting to the malleus was similarly dysmorphic, in some cases with ectopic insertion into the wall of the middle ear cavity (Fig. 4C). In contrast, deletion of *Nr5a2* from limb mesenchyme using *Prrx1-Cre* had no effect on the bones or *Scx-GFP+* tendons of the forelimb and hindlimb (Fig. S4G,H), showing specificity of skeletal and tendon defects to the jaw and middle ear.

In addition to tendon defects, *Nr5a2<sup>NCC</sup>* animals had a complete absence of submandibular and sublingual salivary glands and their connecting ducts at birth (Fig. 4D; Fig. S4J), consistent with these arising from the *Nr5a2*-expressing mandibular domain. These defects are reflected by a complete loss of salivary gland mesenchyme and epithelial invagination at E12.5 (Fig. 4D). The parotid and lacrimal glands arising from the mid-oral and eye field, respectively, were unaffected (Fig. S4J). These findings identify a highly region-specific requirement for *Nr5a2* in development of tendons and glands from the mandibular arch.

### **Single-cell multi-omics analysis of mandibular CNCC defects in *nr5a2* mutants**

We next sought to understand the mechanistic basis by which *Nr5a2* regulates cell fate decisions in the jaw. Given its role in transcriptional regulation, we performed integrated single-nuclei analysis (10X Genomics Multiome) of mRNA expression (snRNAseq) and

assay for transposase accessible chromatin (snATACseq) in *nr5a2*-expressing cells sorted from control (*nr5a2*<sup>mGFP-DBD-del/+</sup>) and mutant (*nr5a2*<sup>mGFP-DBD-del/oz3</sup>) fish heads at 2.5 dpf (Fig. 5A). After filtering for nuclei with high quality reads (see Methods), we recovered 4,304 control and 6,589 mutant cells with a median of 11,505 and 6,546 ATAC fragments and 1,411 and 821 genes per nucleus, respectively. UMAP clustering of integrated RNAseq and ATACseq data from control and mutant heads using Seurat (see Methods), combined with analysis of known cell type markers, identified major clusters of neurons and mesenchyme, consistent with expression of *nr5a2*<sup>mGFP</sup> in both these populations (Fig. S5A,B; Table S1). We also observed clusters of epithelial, vascular, and blood cells, likely representing contaminating cells. We then extracted and combined control and mutant mesenchyme clusters based on co-expression of *fli1a* and *prrx1a*, which resolved into 14 clusters upon sub-clustering (Fig. S5C; Table S1). For detailed analysis, we further extracted a cartilage cluster (*acana*+), a tendon cluster (*tnmd*+), and four mandibular arch mesenchyme clusters (based on co-expression of *dlx2a*, *dlx5a*, and *hand2*) (Fig 5B; Fig. S5C). The six remaining *dlx2a*-; *dlx5a*- mesenchyme clusters, which express lower levels of *nr5a2* (Fig. S5C), may represent the neurocranium mesenchyme that we found also weakly expresses *nr5a2*<sup>mGFP</sup> (Fig. S1B).

Differential analysis of snATACseq data by chromVAR identified that the top DNA-binding motif underrepresented in mutant versus control mandibular mesenchyme accessible regions was Nr5a2, followed by Egr1 (and versions of these) (Fig. 5C; Table S2). Feature plots of mandibular mesenchyme clusters confirmed that, while expression of *nr5a2* persists in mutants, the Nr5a2 binding motif was nearly completely absent in mutant accessible chromatin regions (Fig. 5C; Fig. S5C). Whereas 559 regions displayed reduced accessibility in mutants, with 47% containing Nr5a2 motifs, only 34 regions had increased accessibility, with none containing Nr5a2 motifs (> 1.19 fold change,  $p < 0.01$ ; Fig. 5D; Table S3). We also identified 204 genes that were downregulated in mutants, versus only 80 that were upregulated (> 1.19 fold change,  $p < 0.01$ ; Fig. 5D; Table S1). Gene Ontology analysis of the 204 downregulated genes

identified enrichment for biological processes that included cell adhesion, extracellular matrix organization, negative regulation of transcription, neural crest cell migration, cartilage development, and embryonic viscerocranium morphogenesis (Table S4). Although our data do not support upregulated genes being directly regulated by Nr5a2, we observed increased expression of *igfbp5b* and *ogna* in the mutant perichondrium (Fig. S6A). In contrast, expression of genes involved in regionalization of the mandibular arch mesenchyme along the dorsoventral (*hand2*) and oral-aboral (*pitx1*, *gsc*, *msx1a*) axes were unaffected in *nr5a2* mutants at 1.5 dpf (Fig. S6B), suggesting that Nr5a2 functions largely downstream of initial regional patterning factors. These findings are consistent with a primary requirement for Nr5a2 to initiate or maintain open chromatin in mandibular mesenchyme to activate gene expression.

#### **Identification of direct targets of Nr5a2 for diverse connective tissue fates**

To identify potential Nr5a2 direct targets, we queried chromatin regions that lost chromatin accessibility in mutants, contained predicted Nr5a2 binding sites, and were located within 500 kb of a gene with decreased expression in mutants. The top five genes included *tnksa* (genomically linked to *fgf10a*), *foxp2*, and *cdh6* (Fig. 5D; Table S5). We found *fgf10a*, *foxp2*, and *cdh6* to be co-expressed with *nr5a2* in the mesenchyme and perichondrium posterior to the developing lower jaw cartilage at 2.5 dpf, with *foxp2* and *fgf10a* labelling largely distinct regions within a broader *nr5a2*<sup>+</sup>; *cdh6*<sup>+</sup> domain (Fig. 6A-C; Fig. S6C). Perichondrium is a tissue surrounding the cartilage that is thought to house progenitors for tendon, cartilage, bone, and other connective tissues<sup>31</sup>. In *nr5a2* mutants, *fgf10a*, *foxp2*, and *cdh6* expression was specifically reduced in the mesenchyme of the lower jaw, including the perichondrium associated with Meckel's cartilage (Fig. 6A-C). In *Fgf10*<sup>-/-</sup> mice, all the salivary glands are lost<sup>32</sup>, similar to the loss of the mandibular glands observed in *Nr5a2*<sup>NCC</sup> mice. In keeping with this result, *Fgf10* expression was selectively lost in the mandibular domain of *Nr5a2*<sup>NCC</sup> mice at E12.5 (Fig. 6D).

We next focused on chromatin regions with reduced accessibility in mutants ( $> 1.19$  fold change,  $p < 0.01$ ) that contained predicted Nr5a2 binding sites. An unbiased analysis of the most highly significant regions identified regions near *fgf10a* (#3,  $p = 1.95E-15$ ), *cdh6* (#6,  $p = 7.19E-14$ ), *foxp2* (#10,  $p = 1.66E-12$ ), and *scxa* (#43,  $p = 1.39E-08$ ) (Table S3). Genome views confirmed reduced accessibility of these regions in mutants, and analysis of previously published snATACseq data of 1.5 dpf facial CNCCs<sup>17</sup> identified enriched accessibility of all four regions in the aboral mandibular domain (Fig. 6; Fig. S6F). Moreover, analysis of published chromatin accessibility data at NCC migration stages<sup>33,34</sup> identified that these regions gain accessibility only after migration into the arches (Fig. S6F). When combined with a minimal promoter in transgenic assays, all four regions drove highly specific expression of GFP in the mesenchyme posterior to Meckel's cartilage, partially overlapping with *scxa:mCherry* expression in jaw tendons and ligaments (Fig. 6; Fig. S6D,E). In addition, GFP expression driven by all four regions was completely lost in mutants at 3 and 6 dpf, with the exception of a small amount of residual GFP expression driven by the *scxa* region (Fig. 6; Fig. S6D). These findings are consistent with Nr5a2 directly binding jaw-specific enhancers for *fgf10a*, *cdh6*, *foxp2*, and *scxa* to activate their expression.

## Discussion

Here we uncovered a local and transient redeployment of the pluripotency factor Nr5a2 to preserve CNCC-derived progenitors for alternative non-skeletal fates in the vertebrate jaw and middle ear. Despite substantial differences in the types of structures arising from the aboral domain of the zebrafish and mouse mandibular arch, we found that Nr5a2 has a common role in repressing skeletogenesis and promoting tendon, gland, and potentially other mesenchymal derivatives in this domain. Transplantation rescue in zebrafish and conditional deletion experiments in mouse identified that Nr5a2 functions cell-autonomously in CNCCs for jaw and middle ear development.

In fish, *nr5a2* was required for the accessibility of jaw-specific enhancers linked to uncommitted mesenchyme and tendon development. These enhancers were enriched for Nr5a2 binding sites, suggesting they are direct Nr5a2 targets. It also seems likely that Nr5a2 functions to open rather than simply maintain accessibility of these enhancers, as *nr5a2* CNCC expression is not observed before 1.5 dpf in zebrafish<sup>24</sup> and the Nr5a2 target enhancers studied here do not gain accessibility until after NCC migration<sup>33,34</sup>. These findings are consistent with the recently reported pioneer factor activity of Nr5a2 during zygotic genome activation in mice<sup>35</sup>, although additional experiments will be needed to confirm this in CNCCs.

Our data support a highly localized role of Nr5a2 in the jaw to limit skeletal fate commitment while priming chromatin competency for connective tissue fates such as tendons and glands. The types of mandibular derivatives affected in zebrafish and mice lacking Nr5a2 reflect substantial evolutionary transitions, in particular the striking transformation of the fish jaw joint into the mammalian middle ear<sup>36</sup>. Whereas in zebrafish *nr5a2* mutants the entire Meckel's cartilage was substantially enlarged, in *Nr5a2<sup>NCC</sup>* mice only the proximal portion of Meckel's that forms the malleus cartilage of the middle ear was enlarged. These more localized phenotypes are reflected by the reduced expression domains and less prominent aboral restriction of *Nr5a2* in mouse. In both species, however, the tendons and ligaments normally associated with the affected jaw and middle ear structures were missing or dysmorphic. Nr5a2 therefore functions similarly in fish and mice to repress chondrogenesis and promote tendon and ligament development, yet the requirement of Nr5a2 has shifted from the entire lower jaw of fish to a more localized region of the jaw joint and middle ear of mice.

In addition to enlargement of the malleus cartilage, *Nr5a2<sup>NCC</sup>* mice displayed shortening and thickening of several bones, including the angular process of the mandibular bone, and the tympanic and gonial bones. Whether this also reflects an expansion of the initial skeletogenic domain, which in turn depletes progenitors required for sustained growth, remains to be determined. *Nr5a2<sup>NCC</sup>* mice also had specific loss of the mandible-

associated salivary glands (submandibular and sublingual), yet the lacrimal and parotid glands that form in different regions of the head were unaffected. Interestingly, despite fish lacking salivary glands, a conserved jaw-specific role of Nr5a2 in *fgf10a/Fgf10* regulation could explain the selective loss of mandibular salivary glands in *Nr5a2<sup>NCC</sup>* mice. We also uncovered other predicted Nr5a2 target genes that we did not validate here, such as *itga8* that is required in mandibular mesenchyme to promote continued morphogenesis of endodermal pouch epithelia<sup>37</sup>. Nr5a2 may therefore promote additional connective tissue fates in the mandibular arch beyond tendon, ligament, and salivary gland mesenchyme.

Several of the direct target genes of Nr5a2, including *foxp2* and *cdh6*, are co-expressed with *nr5a2* in the lower jaw perichondrium, a tissue known to contain progenitors for diverse connective tissue fates<sup>31</sup>. However, lineage tracing with *nr5a2<sup>mGFP</sup>*, as well as the finding that Nr5a2 functions non-cell-autonomously to pattern Meckel's cartilage, show that Nr5a2 acts in tenocyte progenitors, rather than a bipotent cartilage-tendon progenitor, to repress chondrogenesis. *Foxp2* has been shown to repress gene expression in the nervous system by closing chromatin<sup>38</sup>, and members of the *Foxp1/2/4* family can inhibit osteogenic differentiation in mouse<sup>39</sup>. One possibility then is that Nr5a2 indirectly represses skeletogenesis through promoting jaw-specific expression of *foxp2*. Alternatively, lower jaw cartilage expansion in *nr5a2* mutants could be an indirect consequence of disrupted tenocyte specification. Consistently, deletion of both *Scleraxis* genes in zebrafish results in a similar loss of tendons and expansion of Meckel's cartilage as seen in *nr5a2* mutants<sup>10</sup>.

Our data argue against redeployment of Nr5a2 in the mandibular arch reflecting re-utilization of the Nr5a2-regulated pluripotency network. In embryonic stem cells, Nr5a2 regulates the expression of *Oct4* and other pluripotency genes<sup>18,20</sup>, in part by binding as a complex with the pluripotency factors *Sox2* and *Klf4*<sup>19</sup>. Although a recent study has shown that *Oct4* and *Sox2* have important roles in early neural crest formation<sup>40</sup>, we had previously shown that zebrafish homologs of *oct4*, *klf4*, and most other pluripotency

genes are not expressed in postmigratory CNCCs<sup>17</sup>. Sox2 and Klf4 motifs are also not strongly enriched in Nr5a2-dependent chromatin regions in CNCCs. Instead, we found that Nr5a2 is repurposed to regulate a largely distinct set of genes in mandibular CNCCs important for perichondrium biology and formation of tendons, ligaments, and glands. Along with previous studies showing that pluripotency factors Sox2 and Oct4 bind targets in neural progenitors<sup>41</sup> and neural crest cells<sup>40</sup> distinct from those in embryonic stem cells, our findings highlight the context-dependent activity of transcription factors associated with pluripotency at later stages of development.

The role of nuclear receptor transcription factors in controlling cell fate decisions in postmigratory CNCCs may be a general theme. Nr2f (COUP-TF) family nuclear receptors have been shown to restrict progenitors from committing to cartilage fates in the upper jaw, thus facilitating later dermal bone formation<sup>42</sup>. A key difference is that Nr2f factors are expressed during initial formation of CNCC mesenchyme and persist in specific jaw regions, whereas *nr5a2* expression initiates only after migration of CNCCs to the mandibular arch. In the future, it will be interesting to examine what makes this class of transcription factor particularly well suited for regulating CNCC potential in diverse contexts.

## **Limitations of the study**

Whereas we show that Nr5a2 is required for chromatin accessibility at jaw-specific enhancers, many of which contain predicted Nr5a2-binding sites, we did not directly test whether Nr5a2 binds and opens these enhancers during development. It will be important to use approaches such as Cleavage Under Targets and Release Using Nuclease (CUT&RUN) sequencing to profile which putative jaw-specific enhancers are directly bound by Nr5a2. Although Nr5a2 was required for jaw tendon patterning, misexpression of Nr5a2 in zebrafish did not result in a clear expansion of the tendon-forming domain. The expression domain of *nr5a2* is also much broader than the tendon-forming domain in the fish jaw. One possibility is that Nr5a2 functions to prime jaw



tendon enhancers through chromatin opening but does not activate them without the appropriate co-factors. For example, it would be interesting to test whether co-expression of Nr5a2 and the tendon-promoting factor Scx would be sufficient to synergistically induce ectopic tendons. In *Nr5a2<sup>NCC</sup>* mice, we observed expansion of cartilage and dysmorphology of bones in the middle ear. Given that Nr5a2 appears to function mainly as an activator and not a repressor of transcription in zebrafish, it remains unclear how Nr5a2 affects skeletal patterning. Lineage analyses of skeletal progenitors in Nr5a2-deficient fish and mice should help inform the cellular bases of skeletal defects, and genetic studies of Nr5a2 target genes such as *foxp2* will be needed to address molecular mechanisms by which Nr5a2 patterns the jaw and middle ear skeleton.

## **Acknowledgements**

We thank Jenna Galloway for *Tg(scxa:mCherry)<sup>fb301</sup>*, the Broad CIRM Center Flow Cytometry Facility for FACS, the CHLA Center for Personalized Medicine Molecular Genomics Core for NGS sequencing, Megan Matsutani and Olivia Ruffins for fish care, and Samantha Brugmann for sharing the protocol of colorimetric whole-mount in situ for mouse embryos. Funding provided by NIDCR R21DE029656 and R35DE027550 to J.G.C. and HHMI Hannah H. Gray Fellows Program to D.T.F.

## **Author Contributions**

H.-J.C. and J.G.C. conceived of experiments. H.-J.C. conducted zebrafish and mouse experiments and data analysis. L.B., J.C.T., and C.J. initiated the categorization of zebrafish phenotypes. H.-J.C., O.M.D., R.R.R., A.E.M., A.S.T., and D.T.F. categorized mouse phenotypes. H.-J.C., R.R.R., and D.T.F. performed the single-nuclei multiome. J.G.C., A.E.M., and A.S.T. obtained funding and oversaw the project. H.-J.C. and J.G.C. wrote the manuscript, and A.E.M., and A.S.T. reviewed and critiqued the manuscript.

## **Declaration of interests**

The authors declare no competing interests.

## Inclusion and diversity

One or more of the authors of this paper self-identifies as an underrepresented ethnic minority in their field of research or within their geographical location. One or more of the authors of this paper received support from a program designed to increase minority representation in their field of research.

## FIGURE LEGENDS

### Figure 1. *Nr5a2* expression within the developing zebrafish and mouse face

(A) Diagrams of zebrafish heads showing pharyngeal arch CNCCs (grey, numbered), facial cartilages (magenta), and tendons and ligaments (pink). Image at right is a ventral view of the lower jaw in transgenic animals at 6 dpf, with cartilage in blue (*col2a1a:GFP*), tendon and ligament in magenta (*scxa:mCherry*), and muscle in white (phalloidin). Ceratohyal cartilage (Ch), Hyosymplectic cartilage (Hs), Intermandibular tendon (Imt), Interopercular–mandibular ligament (Ioml), Mandibulohyoid junction tendon (Mhj), Meckel’s cartilage (M), Palatoquadrate cartilage (Pq).

(B,C) In situ hybridizations show expression of *nr5a2* (green) in mandibular (arrow) and hyoid (arrowhead) arch CNCCs (*dlx2a+*) at 1.5 dpf, and posterior to developing *sox9a+* M and Pq jaw cartilages at 2 and 3 dpf (lateral views in B and ventral view in C).

(D) Ventral views of the jaw at 3 dpf show *nr5a2:membrane-GFP* (mGFP) expression posterior to *col2a1a:mCherry-NTR+* M and Pq chondrocytes and partially overlapping with the tenocyte and ligamentocyte marker *scxa:mCherry* at the Imt, Ioml, and Mhj.

(E) Diagram shows ventral view of jaw region in E11.5 mouse embryo with dashed lines indicating sagittal sections shown below (numbered). Overviews of sagittal sections with DAPI staining only (1, 2 - white). RNAscope in situ hybridizations of boxed regions show *Nr5a2* expression at the posterior boundary of the mandibular (1st) arch and anterior boundary of the hyoid (2nd) arch, posterior to *Sox9+* Meckel’s cartilage and anterior to

Hyoid (H) cartilage. Similar staining was observed in multiple sections. Scale bars = 50  $\mu\text{m}$  (A-D); 500  $\mu\text{m}$  (E). See also Figure S1.

## **Figure 2. Requirement of *nr5a2* for zebrafish lower jaw development**

(A) Heads of 10 dpf zebrafish and flat-mount dissections of the first and second arch skeleton of 6 dpf zebrafish stained with Alcian Blue (cartilage) and Alizarin Red (bone). Arrows denote thickening of Meckel's cartilage (M) in mutants. Branchiostegal ray bone (Br), Ceratohyal cartilage (Ch), Entopterygoid bone (En), Hyosymplectic cartilage (Hs), Opercle bone (Op), Palatoquadrate cartilage (Pq).

(B) Repeat imaging of individual animals shows progressive thickening of Meckel's cartilage (outlined) in mutant versus control *col2a1a:h2az2a-mCherry-2A-EGFP-CAAX*+ fish. H2az2a-mCherry labels nuclei. EGFP-CAAX channel is not shown.

(C) Quantification of Meckel's chondrocyte number. Difference of wild type and mutant chondrocyte numbers was compared by Wilcoxon rank-sum test at each stage. Error bars represent standard error of the mean. \* =  $p < 0.05$ ; \*\*\* =  $p < 0.0001$ .

(D) Repeated imaging of individuals shows thickening of the *col2a1a*:GFP+ Meckel's cartilage and loss of the *scxa*:mCherry+ intermandibular tendon (lmt, white arrow), interopercular–mandibular ligament (loml, yellow arrow), and mandibulohyoid junction tendon (Mhj, arrowhead) in 4/4 mutants compared to 0/3 wild types. Note that the hyoid tendons (far right at 4 dpf) are unaffected in mutants, as is the midline *scxa*:mCherry expression at 2.5 and 3 dpf that does not contribute to tendons by 4 dpf in wild types.

(E) Phalloidin staining (white) shows that the jaw muscles connected to *col2a1a*:GFP+ Meckel's cartilage are highly disorganized in 5/5 mutants compared to 0/8 wild types. Scale bars = 50  $\mu\text{m}$ . See also Figure S2.

**Figure 3. Nr5a2 functions cell-autonomously in zebrafish CNCCs to promote tenocyte at the expense of chondrocyte fate**

(A) In representative confocal sections at 3 dpf, *nr5a2:mGFP-DBD-del*<sup>+</sup> cells contributed to 12±3.9 Meckel's (M) chondrocytes (arrowheads) across 10 mutants (*nr5a2*<sup>mGFP-DBD-del/mGFP-DBD-del</sup>) versus 0.4±0.8 chondrocytes across 12 controls (*nr5a2*<sup>mGFP-DBD-del/+</sup>) ( $p = 4.76E-05$ , Wilcoxon rank-sum test). Reciprocally, *nr5a2:mGFP-DBD-del*<sup>+</sup> cells contributed to 1.3±0.7 *scxa:mCherry*<sup>+</sup> intermandibular tendon (lmt) cells (arrows) in mutants versus 9.6±2.0 in controls ( $p = 7.2E-05$ , Wilcoxon rank-sum test). Mhj, mandibulohyoid junction.

(B) At 2.5 dpf, *nr5a2:mGFP-DBD-del*<sup>+</sup> cells contributed to 6.1±3.5% *col2a1a:mCherry-NTR*<sup>+</sup> Meckel's chondrocytes (arrowhead, inset) across 6 mutants versus 1.2±1.7% chondrocytes across 10 controls ( $p = 0.0198$ , Wilcoxon rank-sum test). Lower magnification images are confocal projections and insets are digital sections. Ch, ceratohyal cartilage.

(C) Schematic shows shield-stage transplantation of BFP<sup>+</sup> (green, *actb2:LOXP-BFP-LOXP-DsRed*) wild-type ectoderm cells into the CNCC precursor domain of *nr5a2* mutant hosts. In 4/4 mutants, unilateral contribution of wild-type CNCCs rescued morphology of Meckel's cartilage (magenta, *col2a1a:h2az2a-mCherry-2A-EGFP-CAAX*<sup>+</sup> in fluorescent images, h2az2a-mCherry channel is not shown; Alcian Blue<sup>+</sup> at right) and muscle organization (white, Phalloidin, in middle panel). Inset shows magnified digital section in which wild-type CNCCs non-cell-autonomously rescued Meckel's cartilage. Note that BFP signal is decreased after the fixation step required for Phalloidin staining. Pq, palatoquadrate cartilage. Scale bars = 50 μm. See also Figure S3.

**Figure 4. CNCC requirement for Nr5a2 in mouse mandibular arch development**

(A) Newborn (P0) skulls of control (*Nr5a2-f/f*) and *Nr5a2*<sup>NCC</sup> (*Wnt1-Cre; Nr5a2-f/f*) mice stained with Alcian Blue (cartilage) and Alizarin Red (bone). Dashed boxes designate

magnified regions shown at right. Mutants display an enlarged malleus cartilage (Ma), and shorter and thicker lower jaw angular process (Ang), tympanic bone (Ty), and gonial bone (G). Consistent phenotypes were seen across 12 wild-type (*Nr5a2-f/+*, *Nr5a2-f/f* or *Wnt1-Cre; Nr5a2-f/+*) and 6 *Nr5a2<sup>NCC</sup>* heads. Condylar process (Con), coronoid process (Cor), incus (In), body of Meckel's cartilage (M), stapes (St).

(B) Angular processes are labeled for tendon (*Scx-GFP*, magenta) and bone (Alizarin Red, green) in whole-mount imaging, and trichrome staining in sagittal sections. Diagrams depict the dysmorphic tendons (arrow) and detached muscle (yellow arrowhead) in 4/4 *Nr5a2<sup>NCC</sup>* mice.

(C) Dissected middle ears and accompanying diagrams show dysmorphology of the *Scx-GFP+* (magenta) tensor tympanic tendon (Ttt, which connects the malleus (blue) to the tensor tympanic muscle (grey)) in *Nr5a2<sup>NCC</sup>* mice. Tendon defects were seen in 6/6 middle ears from *Nr5a2<sup>NCC</sup>* mice, with abnormal connections to the middle ear wall (yellow) in three ears. The abnormal gonial and tympanic bones are visualized by Alizarin Red staining (green).

(D) Trichrome staining of coronal sections shows absence of salivary gland mesenchyme (Mes, red outline) and epithelial invagination (E) at E12.5 in 2/2 *Nr5a2<sup>NCC</sup>* mice. Sagittal sections at birth (P0) show absence of the submandibular gland (SMG), sublingual gland (SLG), and salivary gland duct (asterisk) in 4/4 *Nr5a2<sup>NCC</sup>* newborn (P0) mice. The tongue (T) is unaffected. Scale bars = 500  $\mu$ m. See also Figure S4.

**Figure 5. Single-cell analysis of gene expression and chromatin changes in *nr5a2* mutants**

(A) Image of 2.5 dpf *nr5a2:mGFP+* cells and scheme for jaw dissection (boxed region), FACS, and Multiome analysis. UMAPs show distribution of mandibular mesenchyme from controls and mutants. Scale bar = 50  $\mu$ m.

(B) UMAPs show distribution of tendon, cartilage, and mandibular mesenchyme (Mes1-4) clusters from controls and mutants, and feature plots show expression of tendon (*tnmd*) and cartilage (*acana*) markers.

(C) Feature plots of the Nr5a2 binding motif (predicted by chromVAR) show its absence in mutant accessible chromatin. Top underrepresented motifs in mutants fall into two classes: Nr5a/Esrr and Egr1/Klf9.

(D) Schematic of regions with reduced or increased accessibility in mutants (> 1.19-fold change, *p* value < 0.01). Peaks were filtered based on predicted Nr5a2 motifs. We then intersected peaks with genes within 500 kb showing down or up regulation (> 1.19-fold change, *p* value < 0.01) to identify potential Nr5a2 target genes and their enhancers. See also Figure S5.

**Figure 6. Nr5a2 regulates jaw-specific enhancer accessibility and gene expression for perichondrium and tendon genes**

(A-C) For each gene, feature plots in top left show downregulation of transcripts in mutant (*nr5a2:mGFP-DBD-del/oz3*) versus control (*nr5a2:mGFP-DBD-del/+*) mandibular mesenchyme. Middle left shows genomic tracks of chromatin accessibility, with the Nr5a2 motif-harboring regions with decreased accessibility shown in grey. Bottom left shows feature plots of 1.5 dpf CNCC snATAC data<sup>17</sup> highlighting accessibility of the shaded regions in the aboral mandibular domain. Top right shows fluorescent in situ hybridizations of the mandibular and hyoid arches in ventral views, with *sox9a* expression labeling chondrocytes (A, C) or DAPI labeling all nuclei (B). White arrowheads denote loss of perichondrium expression in mutants, and yellow arrowheads loss of midline *fgf10a* expression. Bottom right shows transgenic lines in which GFP is

driven by the highlighted genomic regions. For each line, GFP expression is observed posterior to Meckel's (M) cartilage and partially overlapping with *scxa:mCherry* in 5/5 wild types and completely lost in 5/5 mutants. Intermandibular tendon (Imt), interopercular–mandibular ligament (Ioml), mandibulohyoid junction tendon (Mhj).

(D) Oral view of in situ hybridizations for *Fgf10* in dissected mandibular arches from control (*Nr5a2-f/+*) and mutant (*Wnt1-Cre; Nr5a2-f/f*) mouse embryos at E12.5. *Fgf10* expression is selectively lost in mandibular domains (arrows). T, tongue.

(E) Top left shows genome tracks of chromatin accessibility at the *scxa* locus, with the region containing *Nr5a2* motifs and having decreased accessibility in mutants highlighted in grey. At top right, feature plot from 1.5 dpf CNCC snATAC data shows accessibility of this region in the aboral mandibular domain. At bottom, transgenic line in which GFP is driven by the highlighted genomic region shows expression in the *scxa:mCherry+* Ioml ligament in 5/5 wild types and loss of Ioml expression in 5/5 *nr5a2<sup>oz3/oz3</sup>* mutants. Scale bars = 50  $\mu\text{m}$  (A-C, E); 500  $\mu\text{m}$  (D). See also Figure S6 for additional examples of transgenic line expression and expanded genomic views of open chromatin.

## STAR METHODS

### Resource availability

#### ***Lead contact***

Requests for material should be directed to J. Gage Crump (gcrump@usc.edu).

#### ***Materials availability***

All transgenic lines and plasmids generated in this study will be available upon request.

### **Data and code availability**

- Single-cell RNA-seq data have been deposited at GEO and are publicly available as of the date of publication. Accession numbers are listed in the key resources table. Microscopy data reported in this paper will be shared by the lead contact upon request.
- No new code has been generated for this study.
- Any additional information required to reanalyze the data reported in this paper is available from the lead contact upon request.

### **Experimental model and subject details**

All experiments on zebrafish (*Danio rerio*) and mouse (*Mus musculus*) were approved by the Institutional Animal Care and Use Committee of the University of Southern California (IACUC protocols #20771 and #21151). Embryos and animals were humanely euthanized for experiments.

#### **Zebrafish**

Zebrafish were raised in vivarium under standard conditions at 28.5°C with health and water conditions monitored daily. Heterozygous mutant adult fish were raised in similar conditions and showed no visible defects, with homozygous mutant embryos produced by breeding for experimental analysis. Published mutant and transgenic lines include: *nr5a2*<sup>oz3 23</sup>; *Tg(sox10:DsRedExpress)*<sup>el10</sup>; *Tg(fli1:GAL4-VP16,myl7:EGFP)*<sup>el360</sup>; *Tg(sox10:EGFP-CAAX)*<sup>el375</sup>; *TgBAC(col2a1a:EGFP)*<sup>el483</sup>; *TgBAC(col2a1a:mCherry-NTR)*<sup>el559</sup>; *Tg(col2a1a:h2az2a-mCherry-2A-EGFP-CAAX)*<sup>el690</sup>; *Tg(scxa:mCherry)*<sup>fb30143</sup>; and *Tg(actb2:LOXP-BFP-LOXP-DsRed)*<sup>sd27</sup> (ubiquitous BFP reporter)<sup>44</sup>. Transgenic lines generated in this study include *Tg(nr5a2:GFP-CAAX)*<sup>el874</sup> (*mGFP*); *Tg(nr5a2:GFP-CAAX-DBD-del)*<sup>el875</sup> (*mGFP-DBD-del*); *Tg(UAS:nr5a2,cryaa:Cerulean)*<sup>el877</sup>; *Tg(foxp2\_p1-Mmu.E1b:GFP, cryaa:Cerulean)*<sup>el887; el888; el889</sup>; *Tg(cdh6\_p1-Mmu.E1b:GFP, cryaa:Cerulean)*<sup>el895; el896; el897</sup>; *Tg(fgf10a\_p1-Mmu.E1b:GFP, cryaa:Cerulean)*<sup>el890; el891; el892</sup>;



and *Tg(scxa\_p2-Mmu.E1b:GFP, cryaa:Cerulean)<sup>el900; el901</sup>*. All transgenic lines generated in this study are on a Tubingen background. Developmental stages and numbers of embryos used are described for each experiment. As zebrafish develop gender differences after the stages studied here, the gender of embryos was undetermined. For *oz3* allele genotyping, genomic DNA was amplified by PCR and digested by restriction enzyme BsrI. Wild type yields cut DNA products, while *oz3* yields uncut product. For the *nr5a2:mGFP-DBD-del* allele, genotyping was based on a reduction in band size due to the 9 bp deletion.

### **Mice**

Mice were raised in vivarium under standard conditions with health conditions monitored daily. All mice are in the C57BL/6 background. Alleles utilized in this study are *Nr5a2-flox* (*Nr5a2<sup>tm1Saki</sup>*, JAX 024054, The Jackson Laboratory), *Wnt1-Cre1*<sup>45</sup>, *Prrx1-Cre* (*Tg(Prrx1-Cre)1Cjt*, JAX 005584, The Jackson Laboratory), and *Scx-GFP* (*Tg(Scx-GFP)1Stzr*)<sup>46</sup>. Developmental stages and numbers of embryos used are described for each experiment. Both male and female embryos were used. To conditionally delete both *Nr5a2* alleles in mutants, *Nr5a2-flox/flox* was bred onto *Wnt1-Cre* or *Prrx1-Cre* drivers and their siblings were used as controls. Adult mice carrying a subset of transgenes and alleles were raised in similar conditions and showed no visible defects, with conditional mutant embryos produced by breeding for experimental analysis.

## **Method details**

### **Zebrafish transgenesis**

To generate *nr5a2:mGFP*, GFP-CAAX sequences were inserted just upstream of the translation start site (ATG) of *nr5a2* by injecting a mix of Cas9 protein (final concentration of 800 ng/μl, Pnabio CP02), two guide RNAs (see Table S6 for sequences, final concentration of 200 ng/μl), and linearized dsDNA (final concentration of 20 ng/μl) of GFP-CAAX flanked by a left homology arm of 1020 bp and right homology

arm of 1196 bp centered around the translation start site. One founder line was identified with mGFP expression recapitulating endogenous *nr5a2* expression. To generate the *nr5a2:mGFP-DBD-del* allele, five guide RNAs targeting the DNA binding domain (DBD) of *nr5a2* were injected with Cas9 protein into *nr5a2:mGFP* embryos. The deletion allele was identified by the smaller band size following PCR amplification, and sequencing identified an in-frame 9 bp deletion that removes a critical zinc finger motif-forming cysteine residue in the DNA-binding domain.

To generate zebrafish transgenic lines, donor plasmids (final concentration of 20 ng/μl) were co-injected with Tol2 transposase RNA (final concentration of 30 ng/μl) into one-cell-stage embryos. To make *UAS:nr5a2* plasmid, the *nr5a2* coding sequence was first amplified from cDNA made from Tübingen mRNA, and then combined with 10X UAS regulatory sequences and polyA entry vectors into a destination plasmid flanked by Tol2 transposase sequences (Tol2kit)<sup>47</sup> and containing the co-selection marker *cryaa:Cerulean* (“eye CFP”) using Gateway cloning (ThermoFisher BP Clonase II 11789020, LR Clonase II plus 12538120). Three independent *UAS:nr5a2* alleles were tested and gave similar phenotypes when combined with *fli1a:Gal4VP16*. To test putative enhancers of *foxp2*, *cdh6*, *fgf10a*, and *scxa*, accessible chromatin regions were cloned from Tübingen genomic DNA into a plasmid containing *Mmu.E1b* as a minimal promoter, GFP, and *cryaa:Cerulean* as a co-selection marker, flanked by Tol2 transposase sequences, using In-Fusion cloning (Takara Bio 638910). Two to three independent founder lines were identified for each construct, and consistent GFP expression patterns were observed in at least three embryos of each allele (see Fig. 6 and Fig. S6E).

### ***mRNA in situ hybridization***

Zebrafish embryos were fixed in 4% PFA/1X PBS at 4°C overnight and dehydrated through MeOH series (25%, 50%, 75% MeOH in PBSTw (0.25% Tween-20 in 1X PBS), 100% MeOH twice) 5 min each and stored in 100% MeOH at -80°C overnight or longer.

In situ probes in this study include digoxigenin-labeled *cdh6*<sup>48</sup>, *gsc*<sup>49</sup>, *igfbp5b*<sup>25</sup>, *msx1a*<sup>50</sup>, *nr5a2*<sup>17</sup>, *pitx1*<sup>25</sup>, and *Fgf10*<sup>27</sup> (GenePaint Set ID MH359); dinitrophenol-labeled *dlx2a*<sup>51</sup>, *hand2*<sup>52</sup>, and *sox9a*<sup>53</sup>; RNAscope probes of *cdh6*, *fgf10a*, *foxp2*, *nr5a2*, *ogna*, *sox9a*, *Nr5a2*, and *Sox9* were synthesized by Advanced Cell Diagnostics. For whole-mount detection of *cdh6*, *dlx2a*, *gsc*, *hand2*, *igfbp5b*, *msx1a*, *nr5a2*, *pitx1*, and *sox9a* by fluorescent in situ, the full protocol is available online (<https://wiki.zfin.org/display/prot/Triple+Fluorescent+In+Situ>) with minor modifications: 1.5 dpf embryos were permeabilized with gentle shaking for 30 min and 2.5 dpf embryos for 1 hr with 1.25 µg/ml protease K. We used 1 ng/µl of each probe, 1:500 of anti-DIG-peroxidase (Roche 11207733910), 1:200 of anti-DNP-peroxidase (Akoya NEL747A001KT), 1:30 of Tyr-Cy3 (Akoya NEL704A001KT), and 1:30 of Tyr-Cy5 (Akoya NEL705A001KT). Counterstain of nuclei by DAPI staining was performed at 4°C overnight.

Whole-mount detection of *cdh6*, *fgf10a*, *foxp2*, *nr5a2*, *ogna*, and *sox9a* in zebrafish and detection of *Nr5a2* and *Sox9* on mouse sections were performed by RNAscope Multiplex Fluorescent Reagent Kit v2 Assay per manufacturer's instructions (Advanced Cell Diagnostics, protocol 323100-USM, and technical note MK 50-016) with optimization. RNAscope on zebrafish embryos was performed in tubes (six 2.5 dpf embryos/ml). Target Retrieval was performed for 20 min at 100°C. We permeabilized 2.5 dpf embryos with Protease Plus for 15 min at 40°C. RNAscope on mouse embryos was performed on paraformaldehyde-fixed paraffin-embedded sections with sample preparation, paraffin embedding, and sectioning.

For *Fgf10* in situs, mandibular arches of E12.5 mouse embryos were dissected and fixed in 4% PFA/1X PBS at 4°C overnight. Colorimetric whole-mount detection of *Fgf10* was performed as described<sup>54</sup>. In brief, embryos were dehydrated through MeOH series and stored at -20°C overnight, rehydrated through MeOH series to PBSTx (0.2% Triton-X in 1X PBS) before permeabilization by 20 µg/ml of protease K for 30 min with gentle shaking at RT (room temperature). Secondary fixation in 4% PFA/0.1%

glutaraldehyde/1X PBS for 30 min was followed by two washes of PBSTx for 10 min at RT and prehyb incubation for 2 hr at 65°C. 1 ng/μl of probe was used for hybridization for 48 hr followed by 2X SSC and 0.2% SSC washes three each for 20 min at 65°C and two KTBT washes for 10 min each at RT. Blocking and anti-DIG-AP Fab incubation (1:2000, Roche 11093274910) were performed in 20% sheep serum/KTBT at 4°C overnight. We then washed five times with KTBT for 1 hr and twice with NTMT for 15 min before color development in 10 μl NBT/BCIP premix stock (Roche 11681451001) per ml of NTMT in the dark. When hybridization signal was optimal, we stopped the reaction with KTBT followed by PBS washes. Similar expression patterns were observed in at least three zebrafish embryos of wild type and mutant unless described in the text and panels. Numbers of mouse embryos examined are described in the figure legends.

### ***Sectioning***

For paraffin sections, we fixed E11.5 or E12.5 whole embryos or dissected newborn mouse heads in 4% PFA/1X PBS at 4°C overnight, followed by decalcification in 0.5 M EDTA (pH 8) (for newborn) and dehydration through EtOH series (1X PBS, two 50% EtOH, two 70% EtOH for 1 hr each, 95% EtOH overnight, 95% EtOH, three 100% EtOH for 1 hr each at RT in the second day, and then 100% EtOH overnight at 4°C). Before embedding with paraffin, samples were infused with Hemo-De (xylene substitute, Electron Microscopy Sciences 23412-01) and paraffin through a series of 50% EtOH/50% Hemo-De, four Hemo-De at RT. Sections were then placed in the vacuum incubator at 65°C and put through a series of 50% Hemo-De/50% paraffin and paraffin three times for 30 min each. After embedding in paraffin, paraffin blocks were left overnight at RT to harden. For mouse embryos, 5 μm thick sections were cut on a Thermo Scientific Shandon Finesse ME+ Microtome. For newborn mouse heads, 8 μm thick sections were cut with a Leica Microtome RM2245. For cryo-sectioning, E16.5 mouse heads were fixed in 4% PFA/1X PBS followed with 1X PBS wash at 4°C for 30 min each, and were then infused with sucrose (10% sucrose overnight and 30% sucrose until sinking at 4°C) and embedded in OCT (with a quick wash of OCT) (Sakura 4583).

Cryo-blocks were frozen on dry ice and stored in  $-80^{\circ}\text{C}$ . For cryo-sections,  $10\ \mu\text{m}$  thick sections were cut on a Leica Cryostat CM3050S.

### ***Trichrome staining***

Staining was performed via standard protocols. Coronal and sagittal paraffin sections were first de-paraffinized and rehydrated through an EtOH series (100%, 90%, 70%, and 50%) to water. The sections were stained with Alcian Blue (1% Alcian Blue 8GX (BDH) in 3% acetic acid, pH 2.5), Ehrlich's hematoxylin (Solmedia), and differentiated in 2.5% phosphomolybdic acid (Acros Organic), with two rinses of water between each solution. Finally, the sections were stained with Sirius red (0.1% Direct Red 80 in saturated aqueous solution of picric acid, Sigma) followed by two 1% Acetic Acid washes prior to mounting and imaging.

### ***Skeletal staining***

For skeletal staining, zebrafish embryos were fixed in 2% PFA/1X PBS for 1 hr and washed with 100 mM Tris (pH 7.5)/10 mM  $\text{MgCl}_2$  for 10 min at RT. We then incubated embryos with Alcian stain (0.04% Alcian Blue (Anatech 862), 100 mM Tris (pH 7.5), 10 mM  $\text{MgCl}_2$ , 80% EtOH) for cartilage staining overnight followed by de-staining in EtOH gradient (80%, 50%, 25% EtOH in 100 mM Tris (pH 7.5)/10 mM  $\text{MgCl}_2$ ) for 5 min each. Embryos were then incubated in 3%  $\text{H}_2\text{O}_2$  /0.5% KOH with open lids under a light source until pigments bleached. To stain bone, we then washed in 25% glycerol/0.1% KOH for 10 min before adding Alizarin stain (0.01% Alizarin Red S (Sigma A5533), 25% glycerol, 100 mM Tris (pH 7.5)) for 30 min. Embryos were de-stained in 50% glycerol/0.1% KOH twice before whole-mount imaging. Zebrafish facial skeletons were dissected with fine insect pins and mounted on microscope slides for flat-mount imaging.

For whole-mount skeletal staining of E14.5 embryos and newborn mice, we skinned newborn animals and removed soft tissues before fixation in 95% EtOH for five days with occasional changes of fresh EtOH at RT. We then added Alcian stain (0.015% Alcian Blue (Alcian Blue 8GX (Sigma A3157), 75% EtOH, 20% Glacial acetic acid) for

one day and de-stained in 95% EtOH for one day, replacing solution once. Soft tissues were cleared with 0.5% KOH for five days before addition of Alizarin stain (0.002% Alizarin Red S (Sigma A5533), 0.5% KOH) for four days. We then de-stained in 1% KOH for one day before transfer into a glycerol gradient (25%, 50%, 75% glycerol / 0.5% KOH and 100% glycerol) one day each for imaging and storage. E14.5 Meckel's cartilages were dissected with fine insect pins and mounted on microscope slides for flat-mount imaging.

Freshly dissected, un-fixed *Scx-GFP*<sup>+</sup> mouse heads were stained in Alizarin stain and washed in PBS for 30 min each. Reported phenotypes were observed in at least three zebrafish or mouse embryos unless described otherwise.

### ***Immunostaining***

For whole-mount immunostaining, zebrafish embryos were fixed in 4% PFA/1X PBS at 4°C overnight and washed by PBS and ddH<sub>2</sub>O each for 5 min. Permeabilization of embryos was performed in cold acetone at -20°C for 10 min, followed by washing in ddH<sub>2</sub>O for 5 min, rehydrating with PBS for 5 min, blocking for 3 hr at RT, a brief wash, and incubation with rabbit anti-phospho-histone H3 (Ser10) (1:200, Santa Cruz Biotechnology), chicken anti-mCherry (1:200, Novus Biologicals NBP2-25158), or chicken anti-GFP (1:200, Abcam ab13970) in 2% goat serum / PBDTx (1% BSA, 1% DMSO, 0.1% Triton-X in 1X PBS, pH 7.3) at 4°C overnight. We then washed three times for 20 min each with PBDTx before incubating with 1:300 secondary antibodies Alexa Fluor 647 anti-rabbit (ThermoFisher A-31573), Alexa Fluor 568 anti-chicken (ThermoFisher A-11041), or Alexa Fluor 488 anti-chicken (ThermoFisher A-11039), as well as DAPI, in 2% goat serum / PBDTx at 4°C overnight. Embryos were washed twice with PBSTx (0.1% Triton-X in 1X PBS) before imaging.

For staining of mouse cryo-sections, slides were rinsed with ddH<sub>2</sub>O, air dried at RT, and fixed in 4% PFA/1X PBS at 4°C for 10 min. Tissues were permeabilized in PBSTx for 10 min and washed twice with PBSTw (0.05% Tween-20 in 1X PBS). We then blocked for 1h at RT before incubating with mouse anti-MF-20 (1:300, Developmental Studies

Hybridoma Bank MF 20), rabbit anti-Sox9 (1:800, Novus Biologicals NBP1-85551), or chicken anti-GFP (1:200, Abcam ab13970) at 4°C overnight. This was followed with incubation of 1:300 secondary antibodies Alexa Fluor 647 anti-mouse (ThermoFischer A-21242), Alexa Fluor 568 anti-rabbit (ThermoFischer A11011), or Alexa Fluor 488 anti-chicken (ThermoFischer A-11039) in 10% FBS/1% BSA/5% goat serum in PBSTw at RT for 1 hr. Slides were rinsed twice with ddH<sub>2</sub>O before mounting and imaging. Numbers of zebrafish and mouse embryos examined are described for each experiment in the figure panels or legends.

### ***Muscle staining***

To stain muscle, zebrafish embryos were fixed in 4% PFA/1X PBS for 1 hr at RT (or at 4°C overnight), and *Scx-GFP+* mouse limbs were left un-fixed. Both samples were permeabilized with 0.5% Triton-X in PBS for at least 1 hr followed by phalloidin staining (1:100 in 1X PBS, Alexa Fluor 647 Phalloidin, ThermoFischer A22287) at 4°C overnight. Samples were rinsed several times with PBS before imaging. Phenotypes were observed in at least three zebrafish and mouse embryos unless described otherwise.

### ***Transplantation***

For CNCC transplants, BFP+ naïve ectoderm from shield-stage *actb2:LOXP-BFP-LOXP-DsRed* donors was transplanted into CNCC-forming regions of shield-stage *col2a1a:h2az2a-mCherry-2A-EGFP-CAAX* hosts. Transplantation was performed unilaterally with one side as control. Embryos were held in place with 2% methylcellulose in Ringer's solution (116 mM NaCl, 2.6 mM KCl, 5 mM HEPES, pH 7.0) on glass slides flooded with Ringer's solution. A fine glass needle was used to move small clumps of cells from donors to hosts. Animals were recovered in embryo medium with 50 U/ml Penicillin and 0.05 mg/ml Streptomycin, selected by contribution of BFP+ cells to pharyngeal arches on one side of the embryo at 1.5 dpf, and imaged at 6 dpf on a confocal microscope before fixation for phalloidin staining of muscle. The same embryos then underwent skeletal staining as described above.

### **Imaging**

Images of live and fixed zebrafish, as well as sections after in situ hybridization, immunostaining, or phalloidin staining were captured on a Zeiss LSM800 confocal microscope using ZEN software. Skeletal staining, freshly dissected mouse tissues (salivary glands, stomach, and intestines), and mouse whole-mount in situs were imaged using a Leica S8APO stereo microscope. Images of flat-mount zebrafish skeletons were captured with a Leica DM2500 compound microscope. Fluorescence images of freshly dissected mouse skeletons after Alizarin Red staining were taken by a Leica MZ16F fluorescence microscope. Trichrome stains of mouse histological sections were imaged by a Nikon Eclipse 80i microscope.

### **Single nuclei isolation**

Zebrafish embryos were screened for *nr5a2:mGFP-DBD-del+* and *scxa:mCherry+* with a fluorescence dissecting microscope and fin clips were collected for PCR genotyping of the mutant *oz3* allele before 2 dpf. Control and mutant heads were decapitated between the eye and ear after anesthesia at 2.5 dpf. Separately for controls and mutants, 160 dissected heads (twenty heads per tube) were washed twice with fresh and iced Ringer's solution followed by dissociation at 28.5 °C for 40 min by mechanical and enzymatic digestion – nutating and pipetting every 5 min in pre-warmed protease solution (0.25% trypsin, 1 mM EDTA (pH 8.0), and 20 mg/mL Collagenase D (from stock of 400 mg/mL Collagenase D in HBSS) in PBS) until full dissociation. The reaction was stopped with 6X stop solution (6 mM CaCl<sub>2</sub> and 30% fetal bovine serum (FBS) in PBS). Dissociated cells were collected by centrifugation for 5 min (2000 rpm at 4 °C) and washed by suspension solution (1% FBS, 0.8mM CaCl<sub>2</sub>, 50 U/ml Penicillin, 0.05 mg/ml Streptomycin in Leibovitz Medium) twice and filtered by cell strainer before sorting. Live cells were fluorescence-activated cell sorted (FACS) to isolate 50,000 GFP+ cells that excluded the cytoplasmic stain Zombie Violet (control) or nuclear stain DAPI (mutant) into 0.04% BSA/ PBS at 4 °C. Nuclei isolation was performed per manufacturer's instructions (10X Genomics, protocol CG000169, low cell input protocol) with optimization for zebrafish mesenchyme. FACS cells were pelleted for 15 min (300 rcf at



4°C) and incubated with lysis buffer for 100 s on ice. Isolated nuclei were washed by Wash buffer and Nuclei buffer and checked for nuclear integrity with a fluorescence confocal microscope with DAPI staining before use in library construction.

### ***Multi-omic library construction, sequencing, and alignment***

Multi-omic libraries of snATACseq and snRNAseq from the same barcoded single nuclei were constructed per manufacturer's instructions (10X Genomics, Chromium Next GEM Single Cell Multiome ATAC + Gene Expression, protocol CG000338). In brief, to capture accessible chromatin and transcripts from the same cells, accessible chromatin regions from isolated nuclei were first tagged by Tn5 transposase. Tagged chromatin and polyadenylated mRNA from the same nuclei were pulled down and barcoded with the same sequences within isolated GEMs to achieve single-nuclei separation. Chromatin fragments were further indexed with sample-specific i7 indexes and linked with Illumina P5 and P7 sequences. Reverse transcription was performed in GEMs to synthesize RNA:DNA hybrids from polyadenylated mRNA. cDNAs were further synthesized, fragmented, and indexed with sample-specific i7 and i5 indexes and linked with Illumina P5 and P7 sequences. Quality control of libraries was assessed with the 4200 TapeStation system and Qubit dsDNA HS assay kit. Libraries were sequenced on Illumina HiSeq (control) or NextSeq (mutant) platforms. For sequencing snATACseq libraries, both Read1 and Read2 were extended to 60 cycles, and for sequencing snRNAseq libraries, Read2 was extended to 102 cycles for longer coverage. Sequencing reads were aligned to customized genome (built with GRCz11.fa, GRCz11.104.gtf, and JASPAR2020.pfm, with addition of GFP-CAAX and mCherry gene information; the same genome build is used for analysis by Seurat/Signac) and peak calling was performed by Cell Ranger ARC v2.0.0 per manufacturer's instructions to generate peak-by-cell and gene-by-cell count matrices.

### ***Multi-omics data analysis***

Multi-omics data were processed by Seurat v4<sup>55</sup> and Signac v1.6<sup>56</sup> packages in Rstudio following the standard workflow with optimization. To first identify the

mesenchyme populations of individual libraries, Cell Ranger ARC-output count matrices in H5 format of individual libraries were used to create Seurat objects by “CreateSeuratObject” and “CreateChromatinAssay” functions. Quality control was performed by setting the thresholds of accessible region counts ( $nCount\_ATAC$ ) < 50000, transcript counts ( $nCount\_RNA$ ) < 7500, ratio of mononucleosome to nucleosome-free region ( $nucleosome\_signal$ ) < 2, and enrichment at TSS ( $TSS.enrichment$ ) > 0.5. In order to compare accessible chromatin regions (peaks) between control and mutant, peaks-called were combined by “disjoin” function that splits peaks into overlapping and non-overlapping regions between the control and mutant libraries and filtered by new peak widths ( $peakwidths$  < 10000 & > 20). The disjoined-peak list was used to recalculate peak-by-cell count matrices by “CreateFragmentObject”, “FeatureMatrix”, and “CreateChromatinAssay” functions. For further analysis of ATAC data (peak-by-cell count matrices), 95% of most common peaks were selected by “FindTopFeatures (min.cutoff = 5)” function. Normalization and linear dimension reduction by LSI were performed by “RunTFIDF”, and “RunSVD” functions. RNA data (gene-by-cell count matrices) were normalized and scaled, and the top 3000 most common genes were selected by “SCTransform” function for dimension reduction by PCA (“RunPCA” function). To cluster cells with ATAC and RNA information in combination, “FindMultiModalNeighbors” (2:20 dimensions of LSI and 1:25 dimensions of PCA were used, with the first dimension of LSI excluded due to its high correlation with sequencing depth), “RunUMAP” ( $nn.name = “weighted.nn”$ ), and “FindClusters” ( $resolution = 0.8$ ,  $graph.name = “wsnn”$ ,  $algorithm = 3$ ) functions. Identities of clusters were identified by differentially enriched genes calculated by “FindAllMarkers” ( $test.use = “wilcox”$  (Wilcoxon Rank Sum test),  $logfc.threshold = 0.25$  (log2 Fold Change),  $return.thresh = 0.01$  ( $p$  value)) function. Clusters 0, 2, 5, 8, 20 of control library and clusters 2, 4, 10, 18 of mutant library were identified as mesenchyme populations for the high expression of *fli1a*, *prrx1a*, and other mesenchyme genes.

“Merge” function was used to combine count matrices of control and mutant mesenchyme clusters. Merged ATAC data were processed by “FindTopFeatures”

(min.cutoff = 10) and LSI linear dimension reduction, and merged RNA data were processed and dimensionally reduced by PCA as described above. 2:30 dimensions of LSI and 1:30 dimensions of PCA were used to cluster cells with both ATAC and RNA information as described above. After filtering for artificial clusters with over- and under-accessible profiles, 14 sub-clusters of mesenchyme were identified and differentially enriched genes were calculated by “FindAllMarkers” (test.use = “wilcox”, logfc.threshold = 0.25, return.thresh = 0.01, min.pct = 0.25). To calculate motif enrichments of each cell by chromVAR <sup>57</sup>, “AddMotifs” was first used to calculate motif enrichments of each accessible chromatin region (peak) followed by “RunChromVAR” to calculate motif activity in each mesenchyme cell. To identify accessibility of chromatin regions correlated with expression of genes whose TSS was located within 500 kb of the chromatin regions, “LinkPeaks” (method = “spearman”, min.cells = 5, pvalue\_cutoff = 0.1, score\_cutoff = 0.02) <sup>58</sup> was performed on merged mesenchyme.

For detailed analysis of mandibular arch clusters, we further extracted a cartilage cluster (*acana+*, cluster 11), a tendon cluster (*tnmd+*, cluster 2), and four mandibular arch mesenchyme (Mes1-4) clusters (*dlx2a+*; *dlx5a+*; *hand2+*; Hox-negative, clusters 8, 4, 7, and 1, respectively). UMAP visualization of mandibular arch clusters was generated by “FindMultiModalNeighbors” and “RunUMAP” using the same parameters as mesenchyme analysis above. To investigate the difference of mutant mandibular arch clusters compared to control, differential analysis was performed. Differential motif enrichments of mutant and control mandibular mesenchyme, excluding cartilage, were calculated by “FindMarkers” (test.use = “wilcox”, mean.fxn = rowMeans, fc.name = “avg\_diff”, logfc.threshold = 0.25 (calculating average difference)) using “chromvar” matrix, differential accessible chromatin regions by “FindAllMarkers” (test.use = ‘LR’ (logistic regression), logfc.threshold = 0.25, return.thresh = 0.01, min.pct = 0.05, latent.vars = ‘nCount\_ATAC’) on “ATAC” matrix, and differential gene expressions by “FindAllMarkers” (test.use = “wilcox”, logfc.threshold = 0.25, return.thresh = 0.01, min.pct = 0.25) on “SCT” matrix. Gene Ontology analysis (GO) of downregulated genes in mutants was performed using DAVID Bioinformatics Resources <sup>59,60</sup>. To identify potential

Nr5a2 direct targets, regions with less or more accessibility in mutants were divided into two groups: those that contain predicted Nr5a2 binding motifs and those that did not. Genes whose expression correlated with the accessibility of the Nr5a2 motif regions (predicted by “LinkPeaks” above) were intersected with genes with decreased or increased expression in mutants. To investigate the accessibility of enhancers in the published 1.5 dpf CNCC snATACseq data <sup>17</sup>, the most overlapping chromatin regions (peaks) were identified and their activities were plotted for visualization.

## Quantification and statistical analysis

Quantification of Meckel’s chondrocyte numbers across time was performed by counting nuclei labeled by the *col2a1a:h2az2a-mCherry-2A-EGFP-CAAX* transgene in serial confocal sections with Fiji software <sup>61</sup>. Quantification of pHH3+ nuclei labeled by the *col2a1a:h2az2a-mCherry-2A-EGFP-CAAX* transgene in wild-type and mutant Meckel’s was counted in serial confocal sections. Wilcoxon rank-sum test was performed to compare the difference of wild-type and mutant chondrocyte numbers at each stage. Numbers of *nr5a2:mGFP-DBD-del+* tenocytes and chondrocytes were counted by membrane-GFP+ cell outlines and chondrocyte numbers by *col2a1a:mCherry-NTR* labeling in serial confocal sections. Wilcoxon rank-sum test was performed to compare the difference of GFP+ tenocyte numbers and GFP+ chondrocyte proportion to total chondrocyte numbers in wild types and mutants. Quantification of Meckel’s chondrocyte and tenocyte numbers in fixed embryos of *fli1a:Gal4VP16; UAS:nr5a2* and single-transgene animals were counted with nuclei labeled by DAPI within cells marked by chondrocyte or tenocyte transgenes across serial confocal sections. Measurements of skeleton and tendon length in newborn mice were measured by Fiji software. Differences across genotypes were calculated by a Tukey’s range test to account for multiple comparisons.

**Table S1. Differentially expressed genes for control *nr5a2:mGFP+* clusters, mutant *nr5a2:mGFP+* clusters, combined control and mutant *nr5a2:mGFP+* mesenchyme clusters, and *nr5a2* mutant mandibular mesenchyme related to Figure 5A, 5D, S5**

**Table S2. Differential DNA-binding motifs in *nr5a2* mutant mandibular mesenchyme, related to Figure 5C**

**Table S3. Differential chromatin accessibility in *nr5a2* mutant mandibular mesenchyme, related to Figure 5D**

**Table S4. GO analysis of downregulated genes in *nr5a2* mutant mandibular mesenchyme, related to Figure 5D**

**Table S5. Differentially accessible chromatin regions in *nr5a2* mutant mandibular mesenchyme associated with differentially expressed genes and Nr5a2 motifs, related to Figure 5D, 6, S6D-F**

**Table S6. Oligonucleotide sequences, related to STAR Methods**

## **References**

1. Chai, Y., Jiang, X., Ito, Y., Bringas, P., Jr., Han, J., Rowitch, D.H., Soriano, P., McMahon, A.P., and Sucov, H.M. (2000). Fate of the mammalian cranial neural crest during tooth and mandibular morphogenesis. *Development* *127*, 1671-1679. 10.1242/dev.127.8.1671.
2. Chen, J.W., and Galloway, J.L. (2014). The development of zebrafish tendon and ligament progenitors. *Development* *141*, 2035-2045. 10.1242/dev.104067.
3. Crump, J.G., Swartz, M.E., Eberhart, J.K., and Kimmel, C.B. (2006). Moz-dependent Hox expression controls segment-specific fate maps of skeletal precursors in the face. *Development* *133*, 2661-2669. 10.1242/dev.02435.

4. Platt, J.B. (1893). Ectodermic origin of the cartilages of the head. *Anat. Anz.* 8, 506-509.
5. Schilling, T.F., and Kimmel, C.B. (1994). Segment and cell type lineage restrictions during pharyngeal arch development in the zebrafish embryo. *Development* 120, 483-494.
6. Anthwal, N., and Thompson, H. (2016). The development of the mammalian outer and middle ear. *J Anat* 228, 217-232. 10.1111/joa.12344.
7. Bi, W., Deng, J.M., Zhang, Z., Behringer, R.R., and de Crombrughe, B. (1999). Sox9 is required for cartilage formation. *Nat Genet* 22, 85-89. 10.1038/8792.
8. Yan, Y.L., Willoughby, J., Liu, D., Crump, J.G., Wilson, C., Miller, C.T., Singer, A., Kimmel, C., Westerfield, M., and Postlethwait, J.H. (2005). A pair of Sox: distinct and overlapping functions of zebrafish sox9 co-orthologs in craniofacial and pectoral fin development. *Development* 132, 1069-1083. 10.1242/dev.01674.
9. Ducy, P., Zhang, R., Geoffroy, V., Ridall, A.L., and Karsenty, G. (1997). Osf2/Cbfa1: a transcriptional activator of osteoblast differentiation. *Cell* 89, 747-754. 10.1016/s0092-8674(00)80257-3.
10. Kague, E., Hughes, S.M., Lawrence, E.A., Cross, S., Martin-Silverstone, E., Hammond, C.L., and Hinitz, Y. (2019). Scleraxis genes are required for normal musculoskeletal development and for rib growth and mineralization in zebrafish. *FASEB J* 33, 9116-9130. 10.1096/fj.201802654RR.
11. Murchison, N.D., Price, B.A., Conner, D.A., Keene, D.R., Olson, E.N., Tabin, C.J., and Schweitzer, R. (2007). Regulation of tendon differentiation by scleraxis distinguishes force-transmitting tendons from muscle-anchoring tendons. *Development* 134, 2697-2708. 10.1242/dev.001933.
12. Chatzeli, L., Gaete, M., and Tucker, A.S. (2017). Fgf10 and Sox9 are essential for the establishment of distal progenitor cells during mouse salivary gland development. *Development* 144, 2294-2305. 10.1242/dev.146019.
13. Bronner, M.E., and LeDouarin, N.M. (2012). Development and evolution of the neural crest: an overview. *Dev Biol* 366, 2-9. 10.1016/j.ydbio.2011.12.042.

14. Fabian, P., and Crump, J.G. (2022). Reassessing the embryonic origin and potential of craniofacial ectomesenchyme. *Semin Cell Dev Biol*. 10.1016/j.semcdb.2022.03.018.
15. Buitrago-Delgado, E., Nordin, K., Rao, A., Geary, L., and LaBonne, C. (2015). Shared regulatory programs suggest retention of blastula-stage potential in neural crest cells. *Science* 348, 1332-1335. 10.1126/science.aaa3655.
16. Zalc, A., Sinha, R., Gulati, G.S., Wesche, D.J., Daszczuk, P., Swigut, T., Weissman, I.L., and Wysocka, J. (2021). Reactivation of the pluripotency program precedes formation of the cranial neural crest. *Science* 371. 10.1126/science.abb4776.
17. Fabian, P., Tseng, K.C., Thiruppathy, M., Arata, C., Chen, H.J., Smeeton, J., Nelson, N., and Crump, J.G. (2022). Lifelong single-cell profiling of cranial neural crest diversification in zebrafish. *Nat Commun* 13, 13. 10.1038/s41467-021-27594-w.
18. Gu, P., Goodwin, B., Chung, A.C., Xu, X., Wheeler, D.A., Price, R.R., Galardi, C., Peng, L., Latour, A.M., Koller, B.H., et al. (2005). Orphan nuclear receptor LRH-1 is required to maintain Oct4 expression at the epiblast stage of embryonic development. *Mol Cell Biol* 25, 3492-3505. 10.1128/MCB.25.9.3492-3505.2005.
19. Heng, J.C., Feng, B., Han, J., Jiang, J., Kraus, P., Ng, J.H., Orlov, Y.L., Huss, M., Yang, L., Lufkin, T., et al. (2010). The nuclear receptor Nr5a2 can replace Oct4 in the reprogramming of murine somatic cells to pluripotent cells. *Cell Stem Cell* 6, 167-174. 10.1016/j.stem.2009.12.009.
20. Pare, J.F., Malenfant, D., Courtemanche, C., Jacob-Wagner, M., Roy, S., Allard, D., and Belanger, L. (2004). The fetoprotein transcription factor (FTF) gene is essential to embryogenesis and cholesterol homeostasis and is regulated by a DR4 element. *J Biol Chem* 279, 21206-21216. 10.1074/jbc.M401523200.
21. Hale, M.A., Swift, G.H., Hoang, C.Q., Deering, T.G., Masui, T., Lee, Y.K., Xue, J., and MacDonald, R.J. (2014). The nuclear hormone receptor family member NR5A2 controls aspects of multipotent progenitor cell formation and acinar

- differentiation during pancreatic organogenesis. *Development* 141, 3123-3133. 10.1242/dev.109405.
22. Stergiopoulos, A., and Politis, P.K. (2016). Nuclear receptor NR5A2 controls neural stem cell fate decisions during development. *Nat Commun* 7, 12230. 10.1038/ncomms12230.
  23. Nissim, S., Weeks, O., Talbot, J.C., Hedgepeth, J.W., Wucherpfennig, J., Schatzman-Bone, S., Swinburne, I., Cortes, M., Alexa, K., Megason, S., et al. (2016). Iterative use of nuclear receptor Nr5a2 regulates multiple stages of liver and pancreas development. *Dev Biol* 418, 108-123. 10.1016/j.ydbio.2016.07.019.
  24. Bertrand, S., Thisse, B., Tavares, R., Sachs, L., Chaumot, A., Bardet, P.L., Escriva, H., Duffraisse, M., Marchand, O., Safi, R., et al. (2007). Unexpected novel relational links uncovered by extensive developmental profiling of nuclear receptor expression. *PLoS Genet* 3, e188. 10.1371/journal.pgen.0030188.
  25. Askary, A., Xu, P., Barske, L., Bay, M., Bump, P., Balczerski, B., Bonaguidi, M.A., and Crump, J.G. (2017). Genome-wide analysis of facial skeletal regionalization in zebrafish. *Development* 144, 2994-3005. 10.1242/dev.151712.
  26. Yuan, Y., Loh, Y.E., Han, X., Feng, J., Ho, T.V., He, J., Jing, J., Groff, K., Wu, A., and Chai, Y. (2020). Spatiotemporal cellular movement and fate decisions during first pharyngeal arch morphogenesis. *Sci Adv* 6. 10.1126/sciadv.abb0119.
  27. Visel, A., Thaller, C., and Eichele, G. (2004). GenePaint.org: an atlas of gene expression patterns in the mouse embryo. *Nucleic Acids Res* 32, D552-556. 10.1093/nar/gkh029.
  28. Hauser, B.R., Aure, M.H., Kelly, M.C., Hoffman, M.P., Chibly, A.M., and Core, G.a.C.B. (2020). Generation of a Single-Cell RNAseq Atlas of Murine Salivary Gland Development. *iScience* 23, 101838. 10.1016/j.isci.2020.101838.
  29. Rossi, A., Kontarakis, Z., Gerri, C., Nolte, H., Holper, S., Kruger, M., and Stainier, D.Y. (2015). Genetic compensation induced by deleterious mutations but not gene knockdowns. *Nature* 524, 230-233. 10.1038/nature14580.



30. Xu, P., Balczerski, B., Ciozda, A., Louie, K., Oralova, V., Huysseune, A., and Crump, J.G. (2018). Fox proteins are modular competency factors for facial cartilage and tooth specification. *Development* 145. 10.1242/dev.165498.
31. Colnot, C., Lu, C., Hu, D., and Helms, J.A. (2004). Distinguishing the contributions of the perichondrium, cartilage, and vascular endothelium to skeletal development. *Dev Biol* 269, 55-69. 10.1016/j.ydbio.2004.01.011.
32. Entesarian, M., Matsson, H., Klar, J., Bergendal, B., Olson, L., Arakaki, R., Hayashi, Y., Ohuchi, H., Falahat, B., Bolstad, A.I., et al. (2005). Mutations in the gene encoding fibroblast growth factor 10 are associated with aplasia of lacrimal and salivary glands. *Nat Genet* 37, 125-127. 10.1038/ng1507.
33. Lukoseviciute, M., Gavriouchkina, D., Williams, R.M., Hochgreb-Hagele, T., Senanayake, U., Chong-Morrison, V., Thongjuea, S., Repapi, E., Mead, A., and Sauka-Spengler, T. (2018). From Pioneer to Repressor: Bimodal foxd3 Activity Dynamically Remodels Neural Crest Regulatory Landscape In Vivo. *Dev Cell* 47, 608-628 e606. 10.1016/j.devcel.2018.11.009.
34. Trinh, L.A., Chong-Morrison, V., Gavriouchkina, D., Hochgreb-Hagele, T., Senanayake, U., Fraser, S.E., and Sauka-Spengler, T. (2017). Biotagging of Specific Cell Populations in Zebrafish Reveals Gene Regulatory Logic Encoded in the Nuclear Transcriptome. *Cell Rep* 19, 425-440. 10.1016/j.celrep.2017.03.045.
35. Gassler, J., Kobayashi, W., Gaspar, I., Ruangroengkulrith, S., Mohanan, A., Gomez Hernandez, L., Kravchenko, P., Kummecke, M., Lalic, A., Rifel, N., et al. (2022). Zygotic genome activation by the totipotency pioneer factor Nr5a2. *Science* 378, 1305-1315. 10.1126/science.abn7478.
36. Gould, S.J. (1990). An earful of jaw. *Natural History* 3190, 12-23.
37. Talbot, J.C., Nichols, J.T., Yan, Y.L., Leonard, I.F., BreMiller, R.A., Amacher, S.L., Postlethwait, J.H., and Kimmel, C.B. (2016). Pharyngeal morphogenesis requires fras1-itga8-dependent epithelial-mesenchymal interaction. *Dev Biol* 416, 136-148. 10.1016/j.ydbio.2016.05.035.

38. Hickey, S.L., Berto, S., and Konopka, G. (2019). Chromatin Decondensation by FOXP2 Promotes Human Neuron Maturation and Expression of Neurodevelopmental Disease Genes. *Cell Rep* 27, 1699-1711 e1699. 10.1016/j.celrep.2019.04.044.
39. Zhao, H., Zhou, W., Yao, Z., Wan, Y., Cao, J., Zhang, L., Zhao, J., Li, H., Zhou, R., Li, B., et al. (2015). Foxp1/2/4 regulate endochondral ossification as a suppresser complex. *Dev Biol* 398, 242-254. 10.1016/j.ydbio.2014.12.007.
40. Hovland, A.S., Bhattacharya, D., Azambuja, A.P., Pramio, D., Copeland, J., Rothstein, M., and Simoes-Costa, M. (2022). Pluripotency factors are repurposed to shape the epigenomic landscape of neural crest cells. *Dev Cell* 57, 2257-2272 e2255. 10.1016/j.devcel.2022.09.006.
41. Peterson, K.A., Nishi, Y., Ma, W., Vedenko, A., Shokri, L., Zhang, X., McFarlane, M., Baizabal, J.M., Junker, J.P., van Oudenaarden, A., et al. (2012). Neural-specific Sox2 input and differential Gli-binding affinity provide context and positional information in Shh-directed neural patterning. *Genes Dev* 26, 2802-2816. 10.1101/gad.207142.112.
42. Barske, L., Rataud, P., Behizad, K., Del Rio, L., Cox, S.G., and Crump, J.G. (2018). Essential Role of Nr2f Nuclear Receptors in Patterning the Vertebrate Upper Jaw. *Dev Cell* 44, 337-347 e335. 10.1016/j.devcel.2017.12.022.
43. Chen, J.W., Niu, X., King, M.J., Noedl, M.T., Tabin, C.J., and Galloway, J.L. (2020). The mevalonate pathway is a crucial regulator of tendon cell specification. *Development* 147. 10.1242/dev.185389.
44. Kobayashi, I., Kobayashi-Sun, J., Kim, A.D., Pouget, C., Fujita, N., Suda, T., and Traver, D. (2014). Jam1a-Jam2a interactions regulate haematopoietic stem cell fate through Notch signalling. *Nature* 512, 319-323. 10.1038/nature13623.
45. Danielian, P.S., Muccino, D., Rowitch, D.H., Michael, S.K., and McMahon, A.P. (1998). Modification of gene activity in mouse embryos in utero by a tamoxifen-inducible form of Cre recombinase. *Curr Biol* 8, 1323-1326. 10.1016/s0960-9822(07)00562-3.

46. Pryce, B.A., Brent, A.E., Murchison, N.D., Tabin, C.J., and Schweitzer, R. (2007). Generation of transgenic tendon reporters, ScxGFP and ScxAP, using regulatory elements of the scleraxis gene. *Dev Dyn* 236, 1677-1682. 10.1002/dvdy.21179.
47. Kwan, K.M., Fujimoto, E., Grabher, C., Mangum, B.D., Hardy, M.E., Campbell, D.S., Parant, J.M., Yost, H.J., Kanki, J.P., and Chien, C.B. (2007). The Tol2kit: a multisite gateway-based construction kit for Tol2 transposon transgenesis constructs. *Dev Dyn* 236, 3088-3099.
48. Liu, Q., Liu, B., Wilson, A.L., and Rostedt, J. (2006). cadherin-6 message expression in the nervous system of developing zebrafish. *Dev Dyn* 235, 272-278. 10.1002/dvdy.20607.
49. Schulte-Merker, S., Hammerschmidt, M., Beuchle, D., Cho, K.W., De Robertis, E.M., and Nüsslein-Volhard, C. (1994). Expression of zebrafish goosecoid and no tail gene products in wild-type and mutant no tail embryos. *Development* 120, 843-852. 10.1242/dev.120.4.843.
50. Akimenko, M.A., Johnson, S.L., Westerfield, M., and Ekker, M. (1995). Differential induction of four msx homeobox genes during fin development and regeneration in zebrafish. *Development* 121, 347-357. 10.1242/dev.121.2.347.
51. Akimenko, M.A., Ekker, M., Wegner, J., Lin, W., and Westerfield, M. (1994). Combinatorial expression of three zebrafish genes related to distal-less: part of a homeobox gene code for the head. *J Neurosci* 14, 3475-3486.
52. Angelo, S., Lohr, J., Lee, K.H., Ticho, B.S., Breitbart, R.E., Hill, S., Yost, H.J., and Srivastava, D. (2000). Conservation of sequence and expression of Xenopus and zebrafish dHAND during cardiac, branchial arch and lateral mesoderm development. *Mech Dev* 95, 231-237. 10.1016/s0925-4773(00)00334-8.
53. Yan, Y.L., Miller, C.T., Nissen, R.M., Singer, A., Liu, D., Kirn, A., Draper, B., Willoughby, J., Morcos, P.A., Amsterdam, A., et al. (2002). A zebrafish sox9 gene required for cartilage morphogenesis. *Development* 129, 5065-5079. 10.1242/dev.129.21.5065.

54. Elliott, K.H., Millington, G., and Brugmann, S.A. (2018). A novel role for cilia-dependent sonic hedgehog signaling during submandibular gland development. *Dev Dyn* 247, 818-831. 10.1002/dvdy.24627.
55. Hao, Y., Hao, S., Andersen-Nissen, E., Mauck, W.M., Zheng, S., Butler, A., Lee, M.J., Wilk, A.J., Darby, C., Zager, M., et al. (2021). Integrated analysis of multimodal single-cell data. *Cell* 184, 3573-3587.e3529. 10.1016/j.cell.2021.04.048.
56. Stuart, T., Srivastava, A., Madad, S., Lareau, C.A., and Satija, R. (2021). Single-cell chromatin state analysis with Signac. *Nat Methods* 18, 1333-1341. 10.1038/s41592-021-01282-5.
57. Schep, A.N., Wu, B., Buenrostro, J.D., and Greenleaf, W.J. (2017). chromVAR: inferring transcription-factor-associated accessibility from single-cell epigenomic data. *Nat Methods* 14, 975-978. 10.1038/nmeth.4401.
58. Ma, S., Zhang, B., LaFave, L.M., Earl, A.S., Chiang, Z., Hu, Y., Ding, J., Brack, A., Kartha, V.K., Tay, T., et al. (2020). Chromatin Potential Identified by Shared Single-Cell Profiling of RNA and Chromatin. *Cell* 183, 1103-1116.e1120. 10.1016/j.cell.2020.09.056.
59. Huang, d.W., Sherman, B.T., and Lempicki, R.A. (2009). Systematic and integrative analysis of large gene lists using DAVID bioinformatics resources. *Nat Protoc* 4, 44-57. 10.1038/nprot.2008.211.
60. Sherman, B.T., Hao, M., Qiu, J., Jiao, X., Baseler, M.W., Lane, H.C., Imamichi, T., and Chang, W. (2022). DAVID: a web server for functional enrichment analysis and functional annotation of gene lists (2021 update). *Nucleic Acids Res.* 10.1093/nar/gkac194.
61. Schindelin, J., Arganda-Carreras, I., Frise, E., Kaynig, V., Longair, M., Pietzsch, T., Preibisch, S., Rueden, C., Saalfeld, S., Schmid, B., et al. (2012). Fiji: an open-source platform for biological-image analysis. *Nat Methods* 9, 676-682. 10.1038/nmeth.2019.



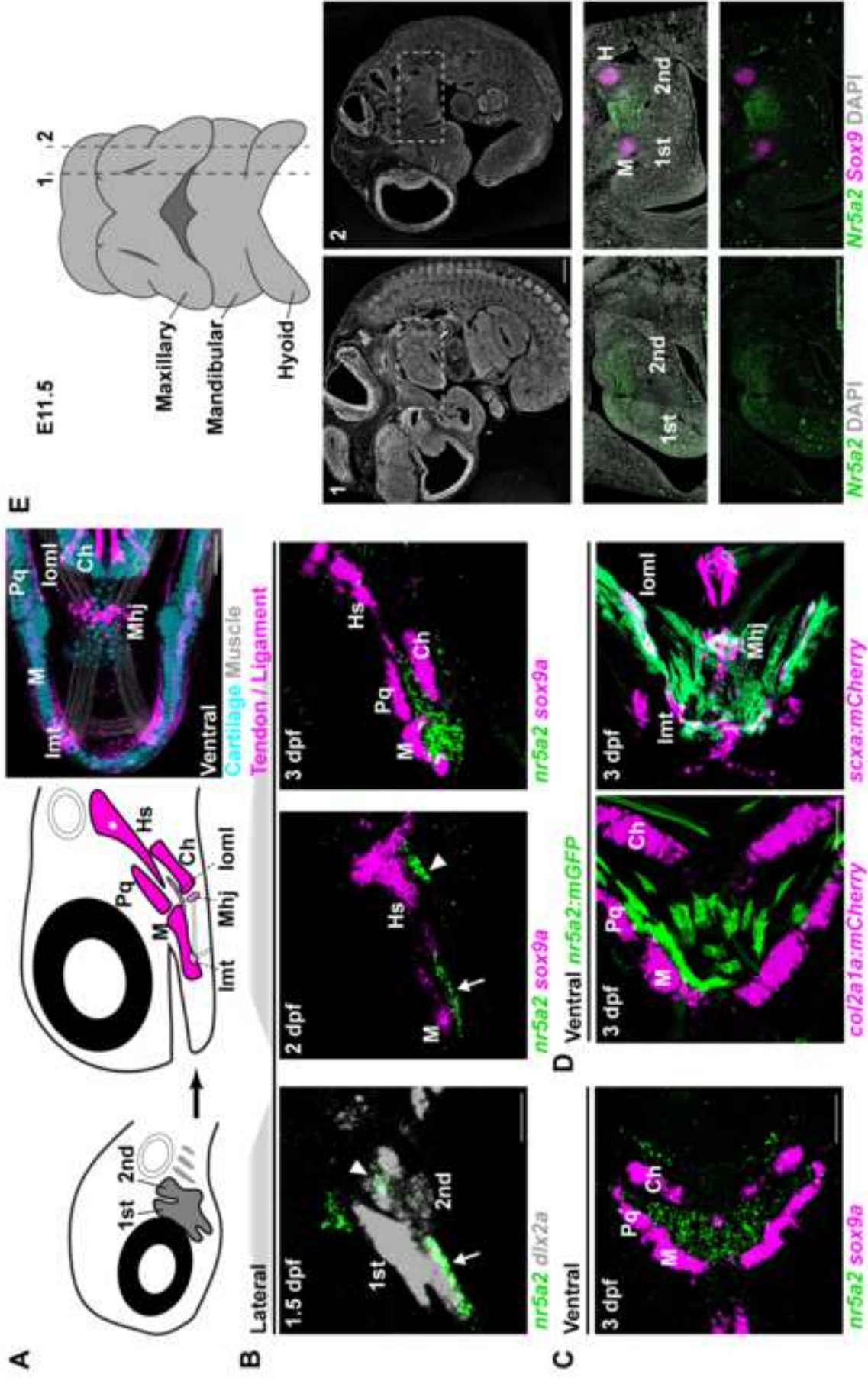
**KEY RESOURCES TABLE**

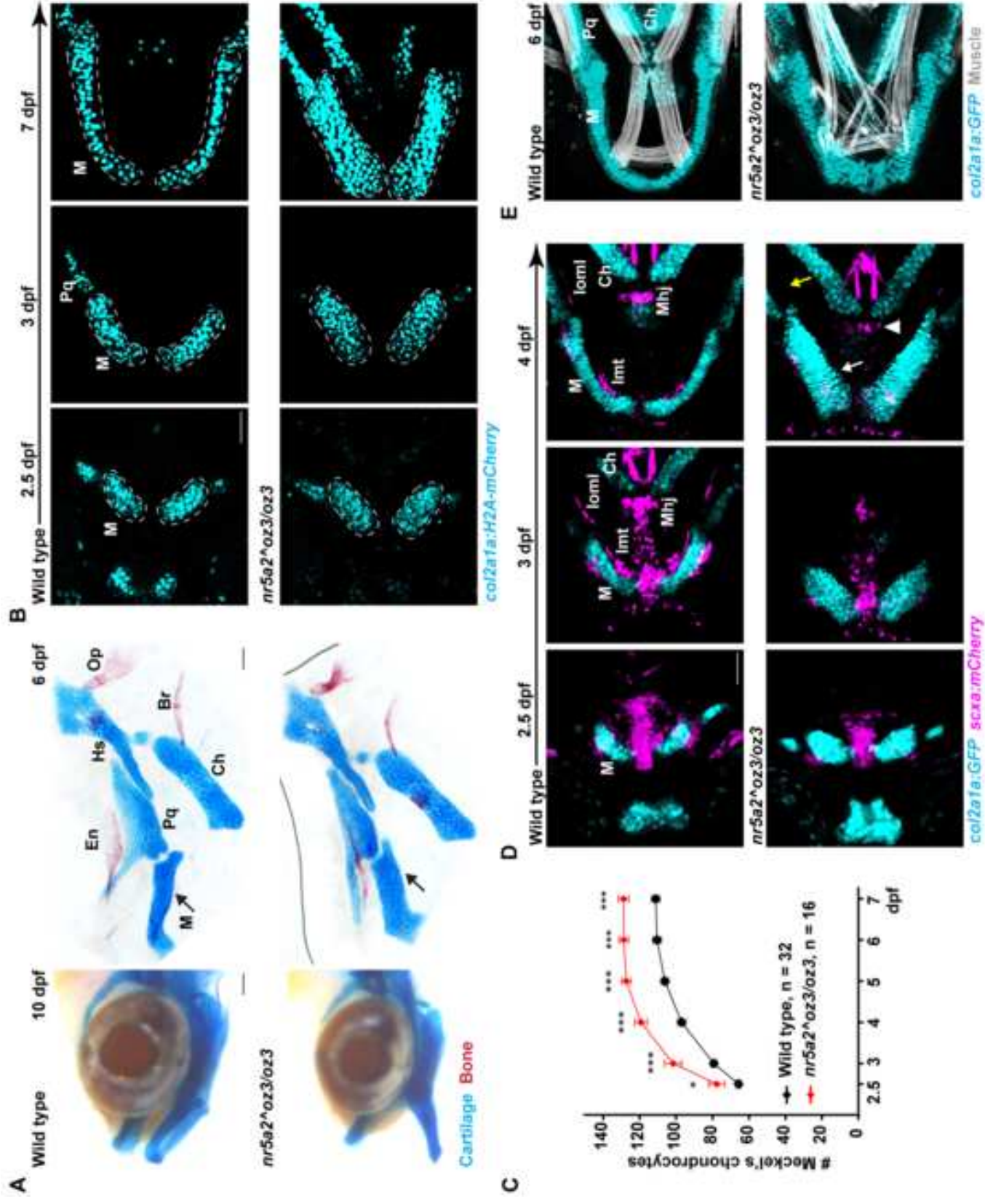
REAGENT or RESOURCE	SOURCE	IDENTIFIER
<b>Antibodies</b>		
rabbit-anti-phospho-histone H3 (Ser10)	Santa Cruz Biotechnology	sc-8656-R
chicken-anti-mCherry	Novus Biologicals	NBP2-25158
chicken-anti-GFP	Abcam	ab13970
mouse-anti-MF-20	Developmental Studies Hybridoma Bank	MF 20
rabbit-anti-Sox9	Novus Biologicals	NBP1-85551
Alexa Fluor 488 anti-chicken	ThermoFisher	A-11039
Alexa Fluor 568 anti-chicken	ThermoFisher	A-11041
Alexa Fluor 568 anti-rabbit	ThermoFisher	A11011
Alexa Fluor 647 anti-rabbit	ThermoFisher	A-31573
Alexa Fluor 647 anti-mouse	ThermoFisher	21242
<b>Chemicals, Peptides, and Recombinant Proteins</b>		
Alexa Fluor 647 Phalloidin	ThermoFisher	A22287
<b>Critical Commercial Assays</b>		
RNAscope Multiplex Fluorescent Reagent Kit v2 Assay	Advanced Cell Diagnostics	Protocol 323100-USM and technical note MK 50-016
Chromium Next GEM Single Cell Multiome ATAC + Gene Expression	10X Genomics	Protocol CG000338
<b>Deposited Data</b>		
Raw sequencing fastq files and Cell Ranger ARC v2.0.0-processed Multiome data in this paper	GEO (Gene Expression Omnibus), this paper	GSE210251
Published scRNAseq of submandibular salivary gland	GEO (Gene Expression Omnibus) (Hauser et al., 2020) <sup>28</sup>	GSE150327
Published scRNA-Seq of mouse mandible	FaceBase (Yuan et al., 2020) <sup>26</sup>	Record ID 1-DTK2
Published ATAC-Seq of zebrafish NCC	GEO (Gene Expression Omnibus) (Trinh et al., 2017) <sup>34</sup>	GSE89670
<b>Experimental Models: Organisms/Strains</b>		
Mouse: Nr5a2-flox: <i>Nr5a2<sup>tm1Sakl</sup></i>	The Jackson Laboratory	JAX 024054

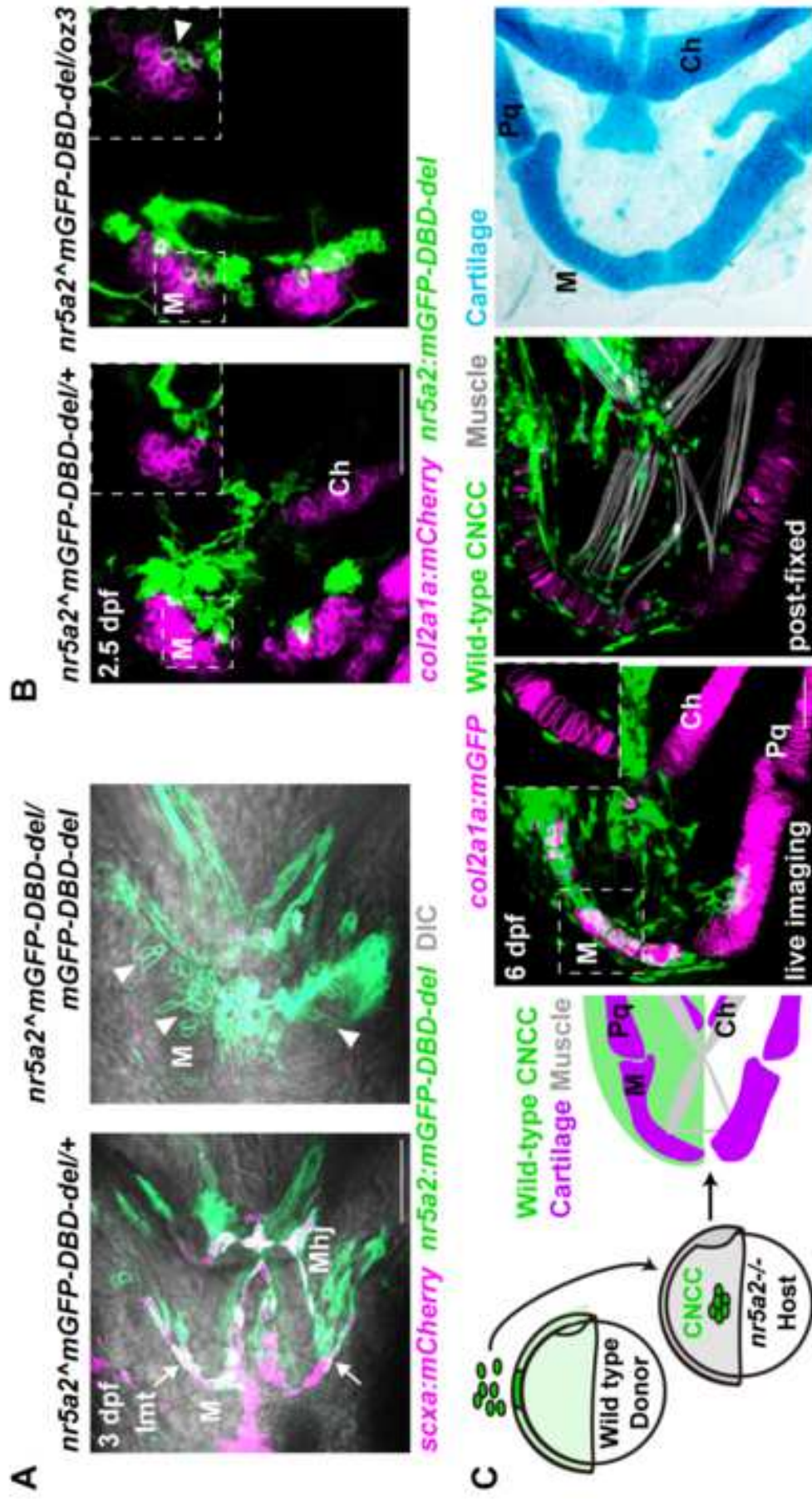
Mouse: Wnt1-Cre: Wnt1-Cre1	(Danielian et al., 1998) <sup>45</sup>	N/A
Mouse: Prrx1-Cre: <i>Tg(Prrx1-Cre)1Cjt</i>	The Jackson Laboratory	JAX 005584
Mouse: <i>Scx-GFP: Tg(Scx-GFP)1Stzr</i>	(Pryce et al., 2007) <sup>46</sup>	N/A
Zebrafish: <i>nr5a2<sup>oz3</sup>: nr5a2<sup>oz3</sup></i>	(Nissim et al., 2016) <sup>23</sup>	oz3
Zebrafish: <i>sox10:dsRed: Tg(sox10:DsRedExpress)</i>	Our lab	e110
Zebrafish: <i>fli1a:GAL4: Tg(fli1:GAL4-VP16,myl7:EGFP)</i>	Our lab	e1360
Zebrafish: <i>sox10:mGFP: Tg(sox10:EGFP-CAAX)</i>	Our lab	e1375
Zebrafish: <i>col2a1a:GFP: TgBAC(col2a1a:EGFP)</i>	Our lab	e1483
Zebrafish: <i>col2a1a:mCherry: TgBAC(col2a1a:mCherry-NTR)</i>	Our lab	e1599
Zebrafish: <i>col2a1a:h2az2a-mCherry-2A-EGFP-CAAX: Tg(col2a1a:h2az2a-mCherry-2A-EGFP-CAAX)</i>	Our lab	e1690
Zebrafish: <i>scxa:mCherry: Tg(scxa:mCherry)</i>	(Chen et al., 2020) <sup>43</sup>	fb301
Zebrafish: <i>actb2:LOXP-BFP-LOXP-DsRed: Tg(actb2:LOXP-BFP-LOXP-DsRed)</i>	(Kobayashi et al., 2014) <sup>44</sup>	sd27
Zebrafish: <i>nr5a2<sup>mGFP</sup>: Tg(nr5a2:GFP-CAAX)</i>	This paper	e1874
Zebrafish: <i>nr5a2<sup>mGFP-DBD-del</sup>: Tg(nr5a2:GFP-CAAX-DBD-del)</i>	This paper	e1875
Zebrafish: <i>UAS-nr5a2: Tg(UAS-nr5a2,cryaa:Cerulean)</i>	This paper	e1877
Zebrafish: <i>foxp2-p1:GFP: Tg(foxp2_p1-Mmu.E1b:GFP, cryaa:Cerulean)</i>	This paper	e1887, e1888, e1889
Zebrafish: <i>cdh6-p1:GFP: Tg(cdh6_p1-Mmu.E1b:GFP, cryaa:Cerulean)</i>	This paper	e1895, e1896, e1897
Zebrafish: <i>fgf10a-p1:GFP: Tg(fgf10a_p1-Mmu.E1b:GFP, cryaa:Cerulean)</i>	This paper	e1890, e1891, e1892
Zebrafish: <i>scxa-p2:GFP: Tg(scxa_p2-Mmu.E1b:GFP, cryaa:Cerulean)</i>	This paper	e1900, e1901
Oligonucleotides		
RNAscope probe: <i>cdh6</i>	Advanced Cell Diagnostics	1225191-C4
RNAscope probe: <i>fgf10a</i>	Advanced Cell Diagnostics	1090101-C1, 1090101-C4
RNAscope probe: <i>foxp2</i>	Advanced Cell Diagnostics	1181381-C1
RNAscope probe: <i>nr5a2</i>	Advanced Cell Diagnostics	578901-C2
RNAscope probe: <i>ogna</i>	Advanced	848241-C4

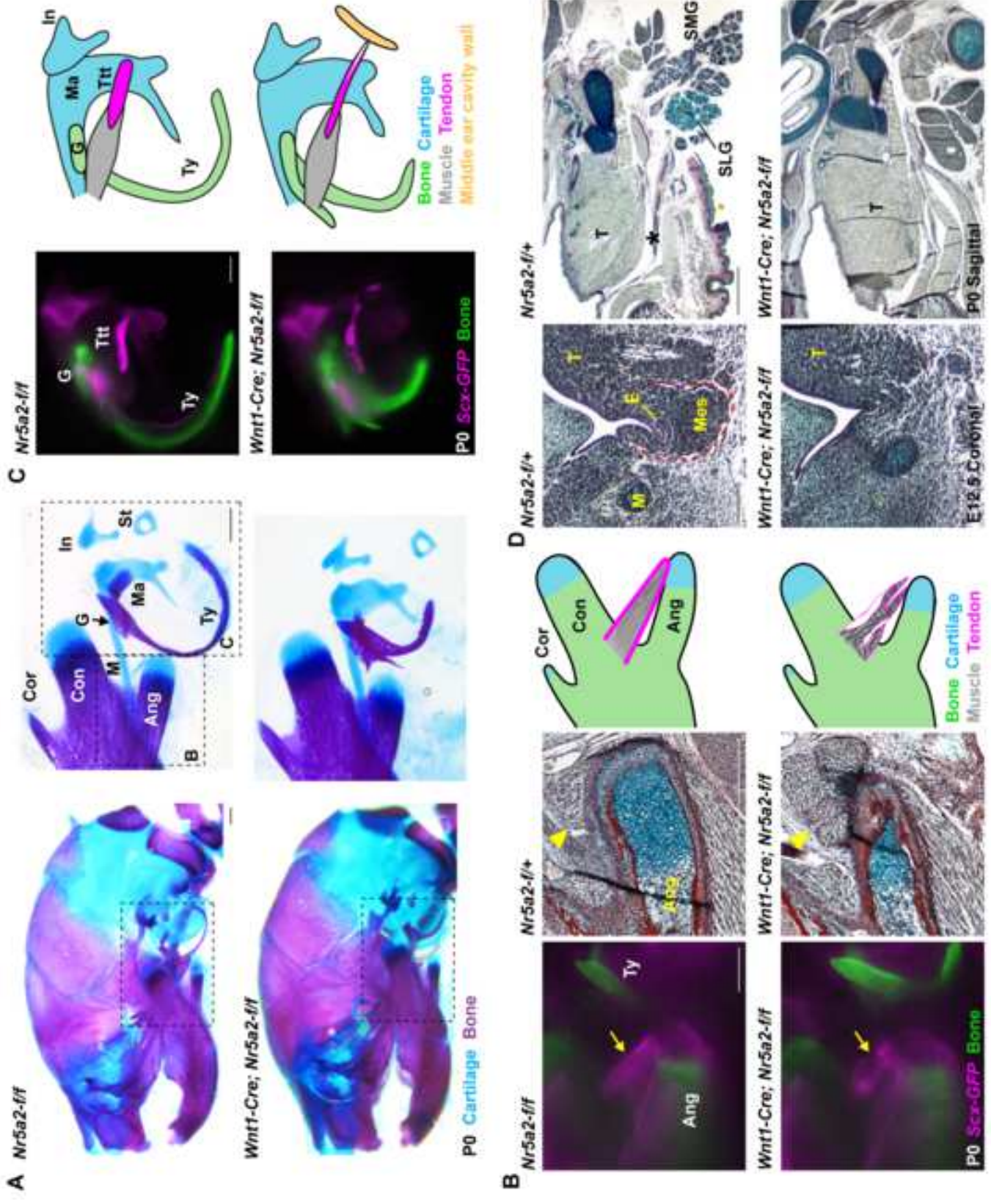
	Cell Diagnostics	
RNAscope probe: <i>sox9a</i>	Advanced Cell Diagnostics	543491-C3
RNAscope probe: <i>Nr5a2</i>	Advanced Cell Diagnostics	543571
RNAscope probe: <i>Sox9</i>	Advanced Cell Diagnostics	401051-C3
guideRNA targeting sequences	Table S6	N/A
In situ hybridization probes	Table S6	N/A
Zebrafish transgenesis primers	Table S6	N/A
Genotyping primers	Table S6	N/A
Software and Algorithms		
Cell Ranger ARC v2.0.0	10X Genomics	<a href="https://support.10xgenomics.com/single-cell-multiome-atac-gex/software/pipelines/latest/what-is-cell-ranger-arc">https://support.10xgenomics.com/single-cell-multiome-atac-gex/software/pipelines/latest/what-is-cell-ranger-arc</a>
Seurat v4	(Hao et al., 2021) <sup>55</sup>	<a href="https://satijalab.org/seurat/">https://satijalab.org/seurat/</a>
Signac v1.6	(Stuart et al., 2021) <sup>56</sup>	<a href="https://satijalab.org/signac/">https://satijalab.org/signac/</a>
chromVAR	(Schep et al., 2017) <sup>57</sup>	<a href="https://greenleaflab.github.io/chromVAR/">https://greenleaflab.github.io/chromVAR/</a>
LinkPeaks	(Ma et al., 2020) <sup>58</sup>	N/A
DAVID Bioinformatics Resources	(Huang et al., 2009) <sup>59</sup> ; (Sherman et al., 2022) <sup>60</sup>	<a href="https://david.ncifcrf.gov/">https://david.ncifcrf.gov/</a>
Fiji	(Schindelin et al., 2012) <sup>61</sup>	<a href="https://fiji.sc">https://fiji.sc</a>

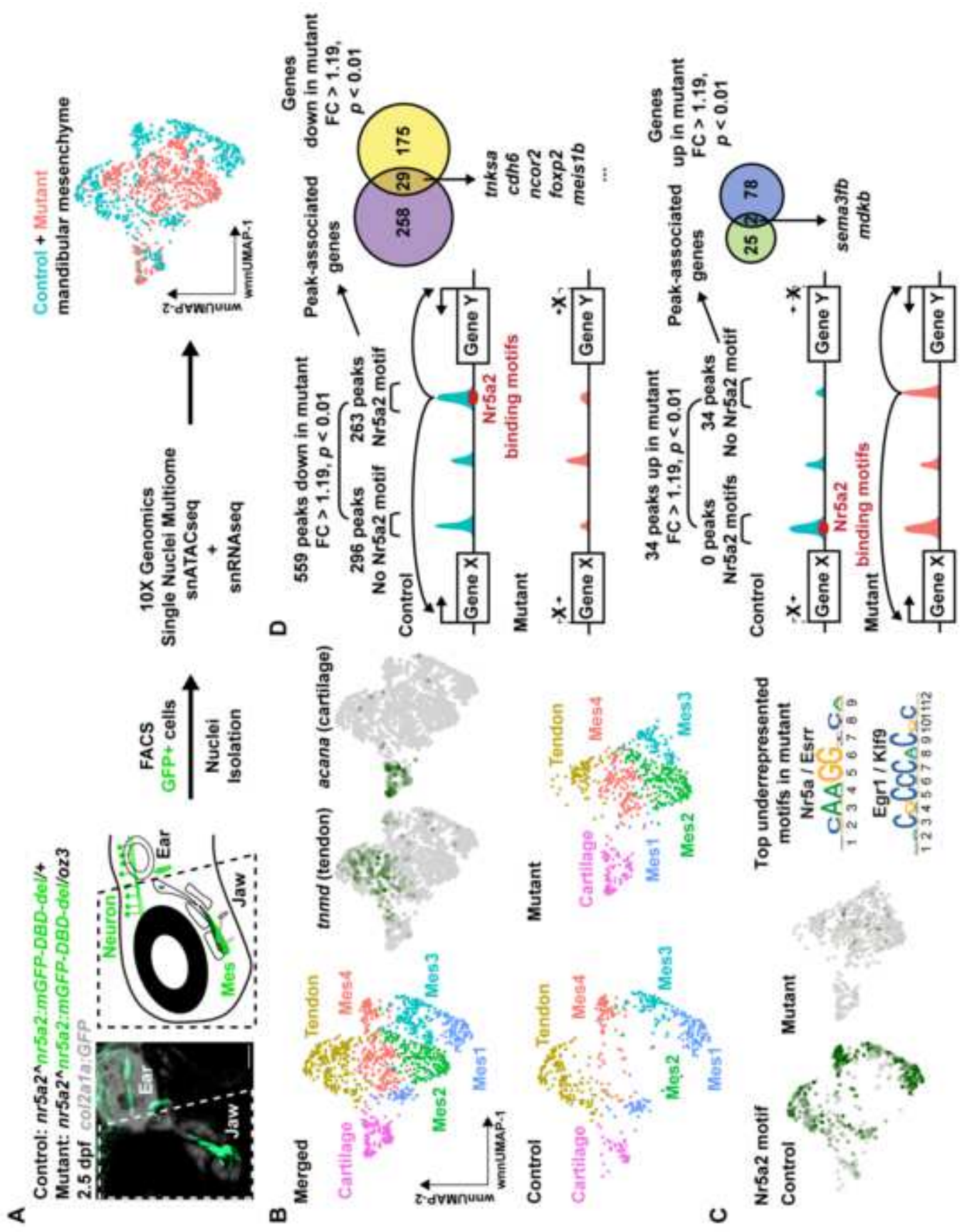


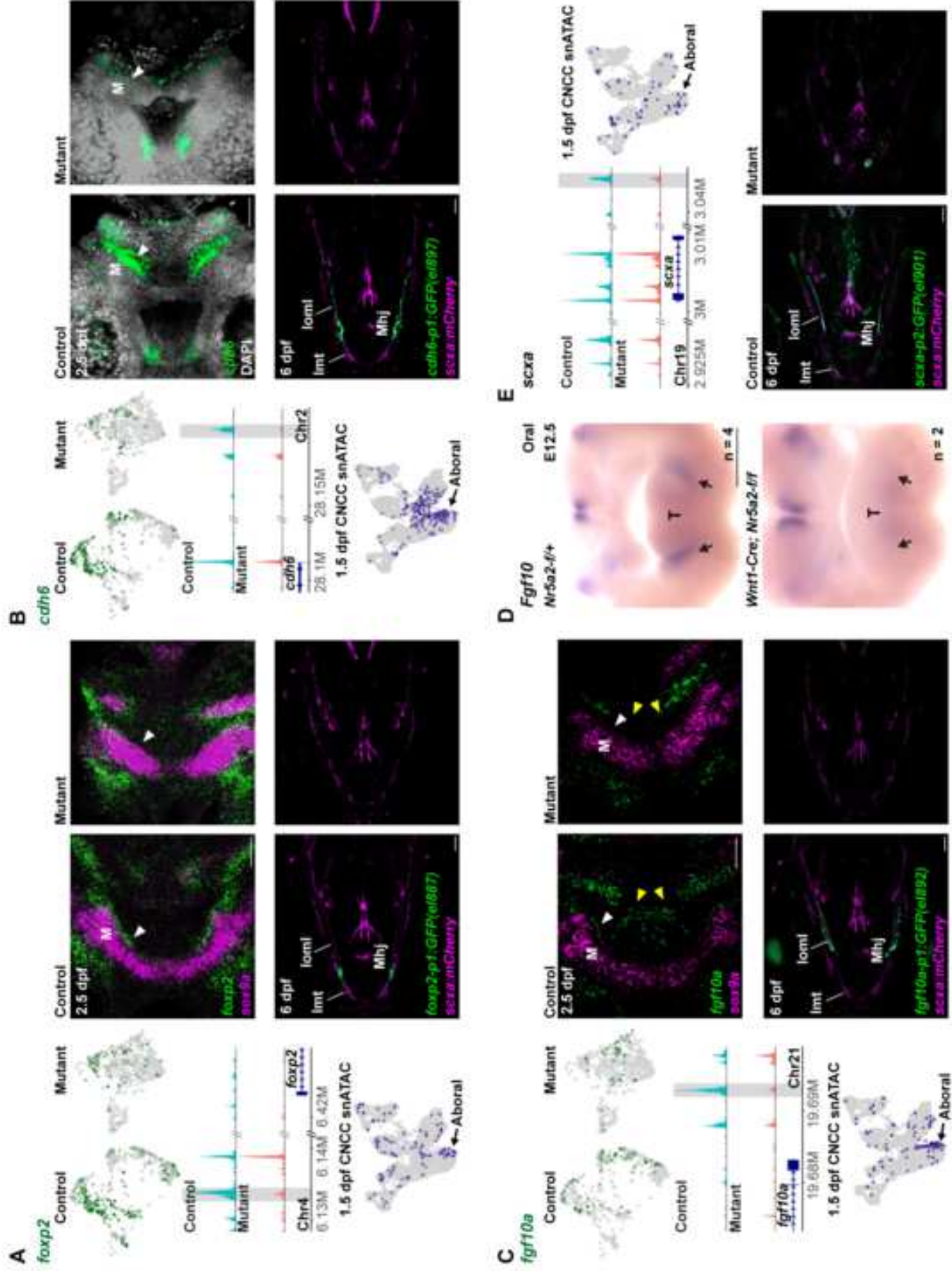












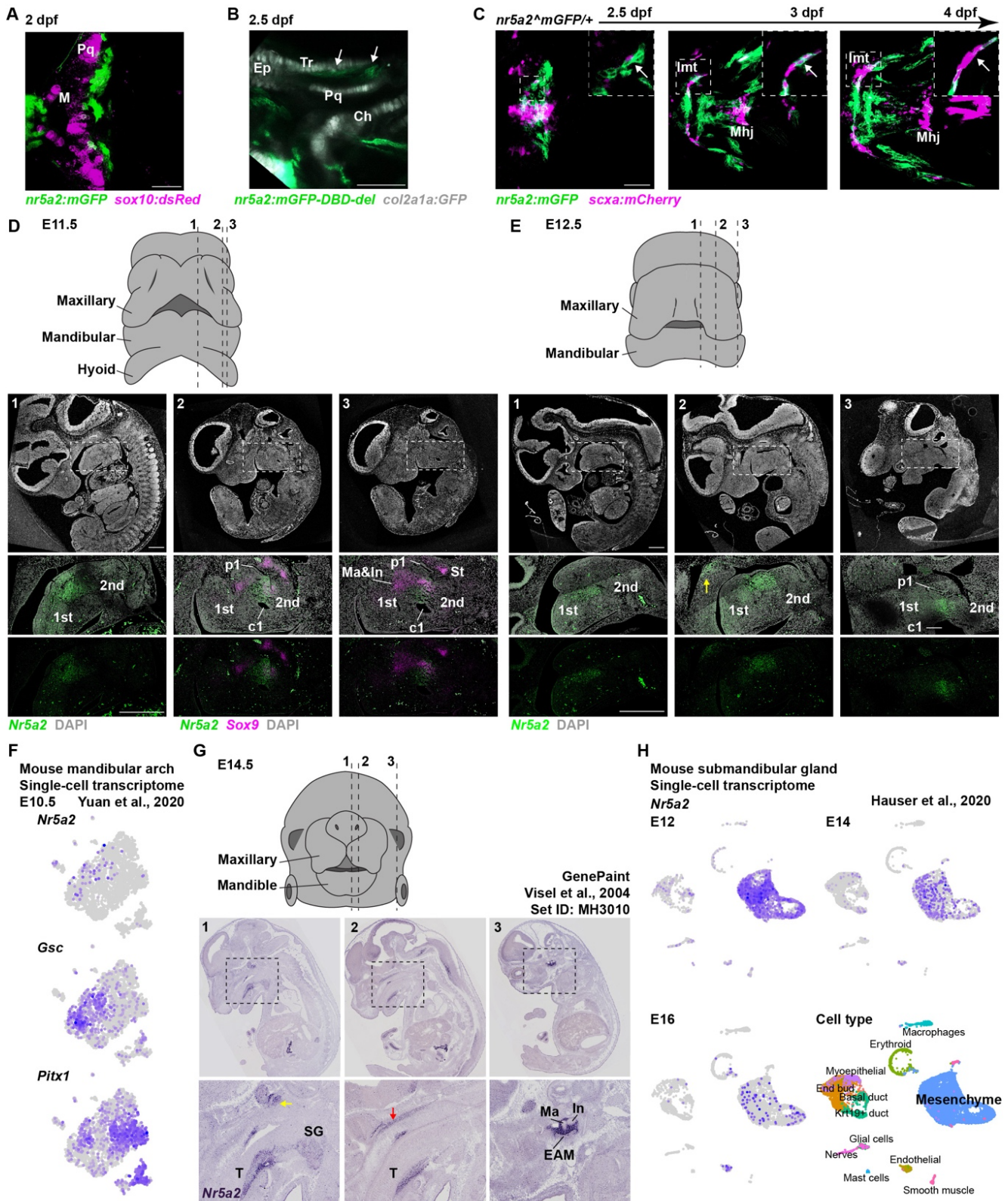


**Figure S1. Detailed facial expression of *nr5a2<sup>mGFP</sup>* in zebrafish and *Nr5a2* in mouse, related to Figure 1**  
 (A) At 2 dpf, confocal image in ventral view shows that *nr5a2<sup>mGFP</sup>* (green) labels mesenchyme posterior to Meckel's (M) and palatoquadrate (Pq) cartilages (magenta).

(B) At 2.5 dpf, confocal image of the neurocranium shows weak *nr5a2:mGFP* expression in mesenchyme (arrows) adjacent to the ethmoid plate (Ep) and trabecula (Tr) cartilages (*col2a1a:GFP+*, grey). Ch, ceratohyal cartilage.

(C) Repeated live imaging shows the emergence of lower jaw *scxa:mCherry+* tenocytes (boxed regions, arrows) from a broader domain of *nr5a2:mGFP+* mesenchyme at intermandibular (lmt) and mandibulohyoid junction (Mhj) tendons in wild type (*nr5a2<sup>mGFP/+</sup>*), with *nr5a2:mGFP* being downregulated as *scxa:mCherry+* jaw tenocytes mature. Lower magnification images are confocal projections and insets are digital sections. Scale bars = 50  $\mu\text{m}$  (A-C).

(D and E) Diagrams show ventral views of the jaw region in mouse embryos at E11.5 and E12.5. Numbers and dashed lines indicate locations of sagittal sections below, with lower magnification views stained with DAPI only to label nuclei. RNAscope in situ hybridizations of boxed regions show *Nr5a2* expression (green), with some sections also showing *Sox9* expression (magenta) to highlight chondrogenic condensations. Expression of *Nr5a2* is seen in the aboral-proximal domain of the mandibular (1st) arch, extending into the hyoid (2nd) arch, and between the first pharyngeal cleft (c1) and first pharyngeal pouch (p1) in mesenchyme associated with the middle ear-forming region. Expression is also seen in the cranial base (yellow arrow). Similar expression was observed in multiple sections. Incus (In), malleus (Ma), stapes (St). Scale bars = 500  $\mu\text{m}$  (D, E).

(F) Published single-cell transcriptome data of E10.5 mandible [S1] show cells with *Nr5a2* transcripts overlapping with transcripts for an aboral marker (*Gsc*) and largely non-overlapping with an oral marker (*Pitx1*).

(G) Diagram shows ventral view of the jaw region in E14.5 mouse embryo and locations of sagittal sections from the GenePaint database [S2]. Magnified regions of boxed areas show *Nr5a2* mesenchymal expression in (1) salivary gland (SG) mesenchyme underneath the tongue (T) and in the cranial base (yellow arrow), (2) mid palate (red arrow), and (3) mesenchyme associated with the malleus (Ma) and incus (In) of the middle ear and external auditory meatus (EAM).

(H) Published single-cell transcriptome datasets of E12, E14, and E16 submandibular salivary glands [S3] show specific expression of *Nr5a2* in the gland mesenchyme cluster. Expression progressively diminishes from E12 to E16.



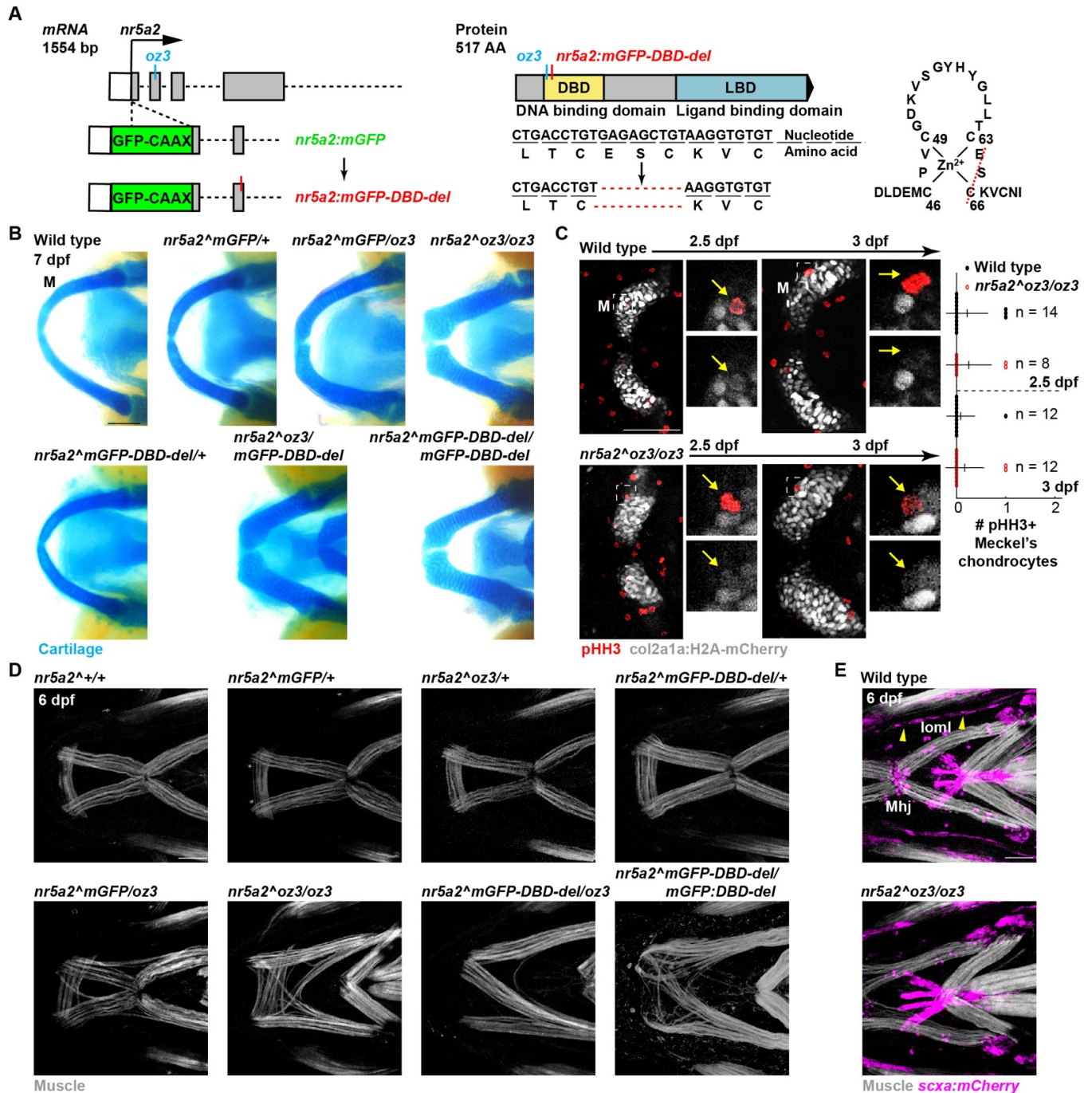


**Figure S2. Characterization of *nr5a2* alleles and cell proliferation assays, related to Figure 2**

(A) Schematic of *nr5a2* alleles. *nr5a2<sup>oz3</sup>* is a frameshift mutation resulting in premature truncation of the DNA binding domain (DBD). GFP-CAAX was inserted at the translation start site to generate *nr5a2<sup>mGFP</sup>*. In-frame deletion of a critical zinc finger motif-forming cysteine residue in the DBD generated *nr5a2<sup>mGFP-DBD-del</sup>*.

(B) Alcian Blue staining shows Meckel's cartilages (M) of wild type and various *nr5a2* mutant allele combinations; the ethmoid plate cartilage is out of focus. Hypomorphic allele *nr5a2<sup>mGFP</sup>* over *oz3* displays a slight thickening of Meckel's cartilage, compared to striking enlargement of Meckel's cartilage in various combinations of *nr5a2<sup>oz3</sup>* and *nr5a2<sup>mGFP-DBD-del</sup>* alleles.

(C) Confocal sections of Meckel's cartilages in wild type and *nr5a2* mutants are shown in ventral views. Anti-phospho-Histone-H3 staining (red, pHH3) shows proliferating chondrocytes labeled by H2az2a-mCherry (white, *col2a1a:h2az2a-mCherry-2A-EGFP-CAAX*+, EGFP-CAAX channel not shown). Yellow arrows in insets

of boxed regions denote rare pHH3+ chondrocytes. Quantification to the right shows no changes in proliferation of Meckel's chondrocytes in *nr5a2* mutants at 2.5 and 3 dpf ( $p = 0.8879$  and  $0.5797$  by Wilcoxon rank-sum test). Error bars represent standard error of the mean.

(D) Phalloidin staining of lower jaw muscle fibers (white) in ventral view shows mild muscle defects in *nr5a2*<sup>mGFP</sup> over *oz3* and severe muscle disorganization in various combinations of *nr5a2*<sup>oz3</sup> and *nr5a2*<sup>mGFP-DBD-del</sup> alleles.

(E) In 12/13 *nr5a2* mutants (5 *nr5a2*<sup>oz3/oz3</sup> and 8 *nr5a2*<sup>mGFP-DBD-del/oz3</sup>), ventral views of *scxa:mCherry* (magenta) with Phalloidin staining of muscle (white) reveal loss of the interopercular–mandibular ligament (Ioml, arrowheads in control) and mandibulohyoid junction tendon (Mhj). Note the midline hyoid tendons are unaffected in mutants. Scale bars = 50  $\mu$ m.

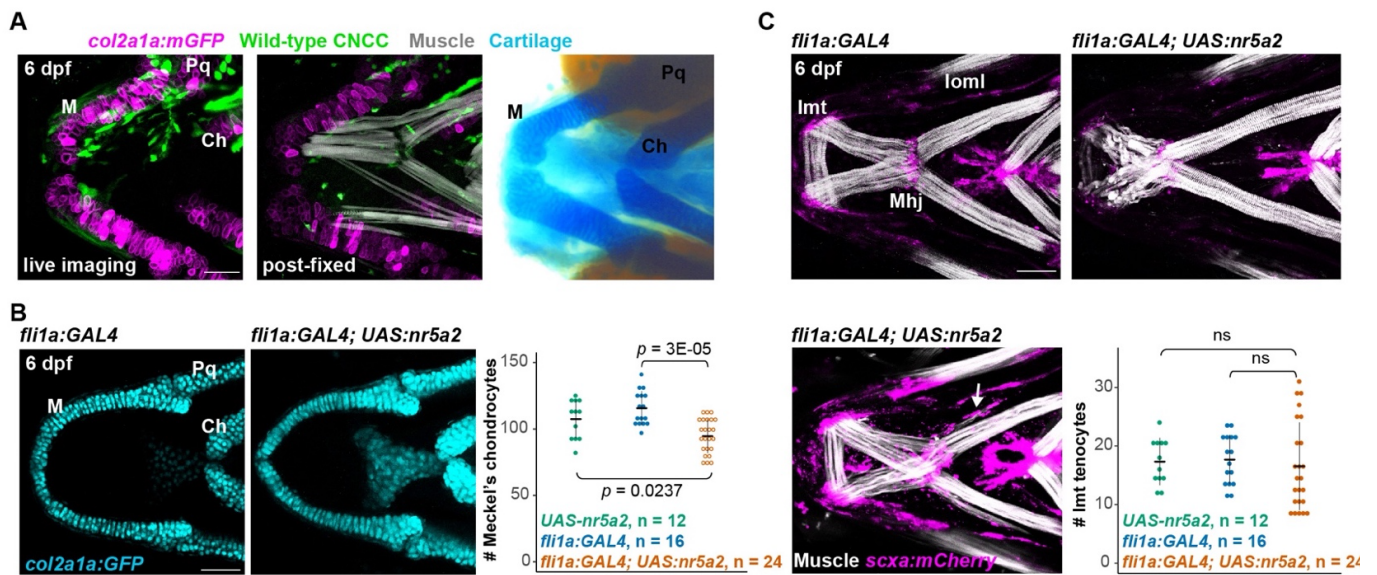


**Figure S3. Nr5a2 functions in CNCCs and is sufficient to suppress chondrogenesis and disrupt tendon formation in the zebrafish lower jaw, related to Figure 3.**

(A) Additional example of shield-stage transplantation of wild-type ectoderm cells into the CNCC precursor domain of *nr5a2* mutant host. Shown in ventral view, contribution of BFP+ wild-type CNCCs (*actb2:LOXP-BFP-LOXP-DsRed*, green) to the left side of the jaw (top) rescued morphology of Meckel's cartilage (M, magenta, *col2a1a:h2az2a-mCherry-2A-EGFP-CAAX* in fluorescent images, *h2az2a-mCherry* channel is not shown; Alcian Blue+ at right) only on the transplanted side. Organization of muscles (Phalloidin, white) was also rescued only on the transplanted side, with muscles appearing to connect to wild-type BFP+ tenocytes. Note that BFP signal is decreased after the fixation step required for Phalloidin staining. Ceratohyal cartilage (Ch), palatoquadrate cartilage (Pq).

(B) Ventral views of Meckel's cartilages labeled by *col2a1a:GFP*. CNCC-specific misexpression of *nr5a2* in *fli1a:Gal4VP16; UAS:nr5a2* animals results in a more pointed morphology of Meckel's cartilages. Quantification shows a mild reduction in Meckel's chondrocyte number in *fli1a:Gal4VP16; UAS:nr5a2* animals versus single-positive *fli1a:Gal4VP16* or *UAS:nr5a2* controls.

(C) Ventral views show the jaw muscles labeled by Phalloidin (white) and the intermandibular tendon (Imt), interopercular–mandibular ligament (Ioml), and mandibulohyoid junction tendon (Mhj) labeled by *scxa:mCherry* (magenta). CNCC-specific misexpression of *nr5a2* in *fli1a:Gal4VP16; UAS:nr5a2* animals results in disorganized Imt and Mhj tendons and associated muscles; arrow in example below shows ectopic *scxa:mCherry*+ cells connecting to a stray muscle fiber. Quantification reveals no changes in Imt tenocyte number in *fli1a:Gal4VP16; UAS:nr5a2* animals versus single-positive *fli1a:Gal4VP16* or *UAS:nr5a2* controls. DAPI staining (not shown) was performed to identify individual chondrocyte or tenocyte nuclei. Statistical difference of chondrocyte or tenocyte numbers across genotypes was compared by Tukey's range test. ns, not significant. Error bars represent standard error of the mean. Scale bars = 50  $\mu$ m.

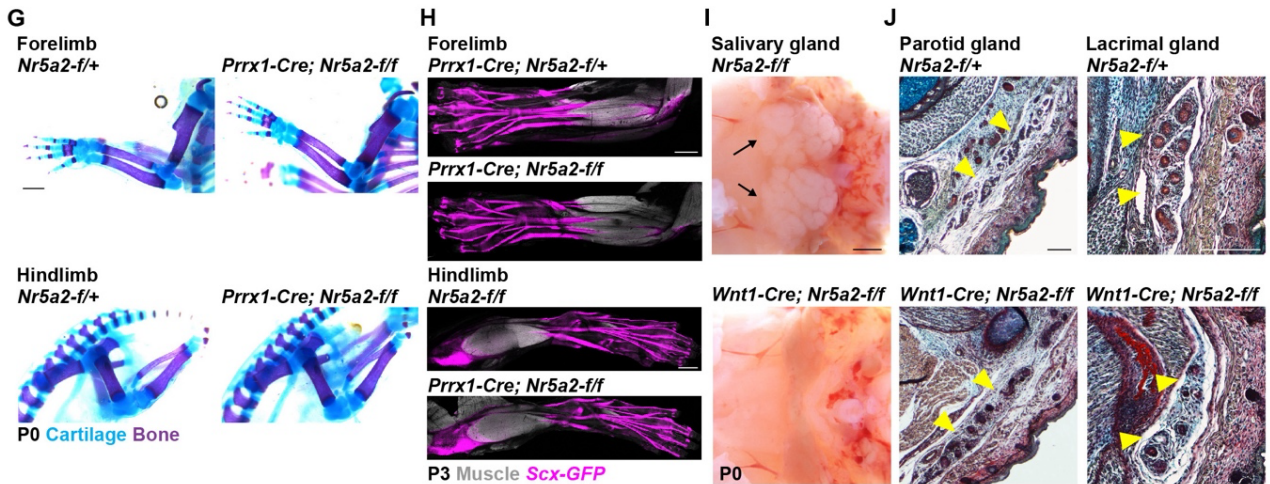
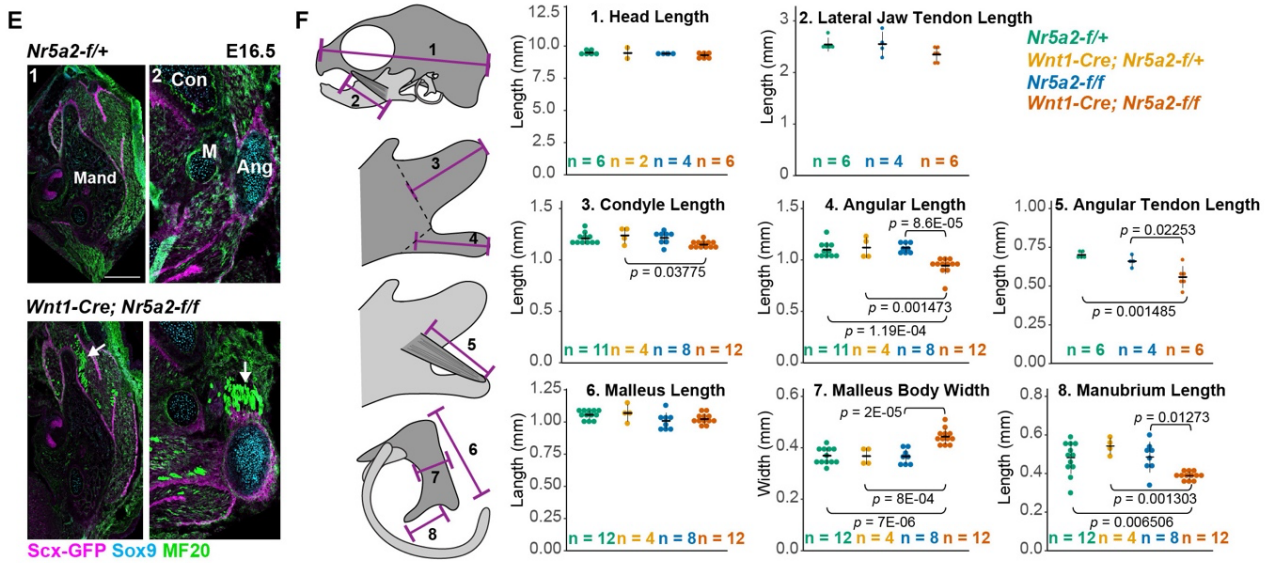
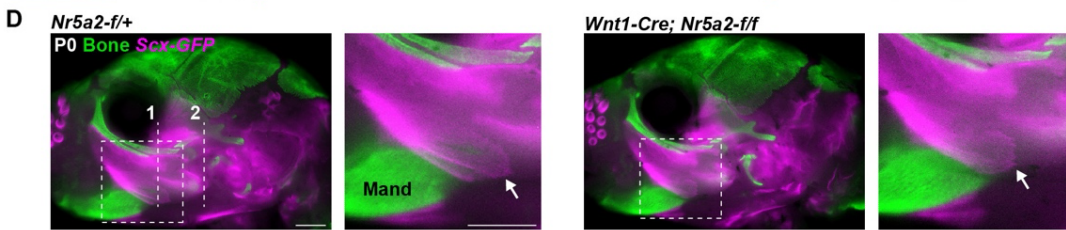
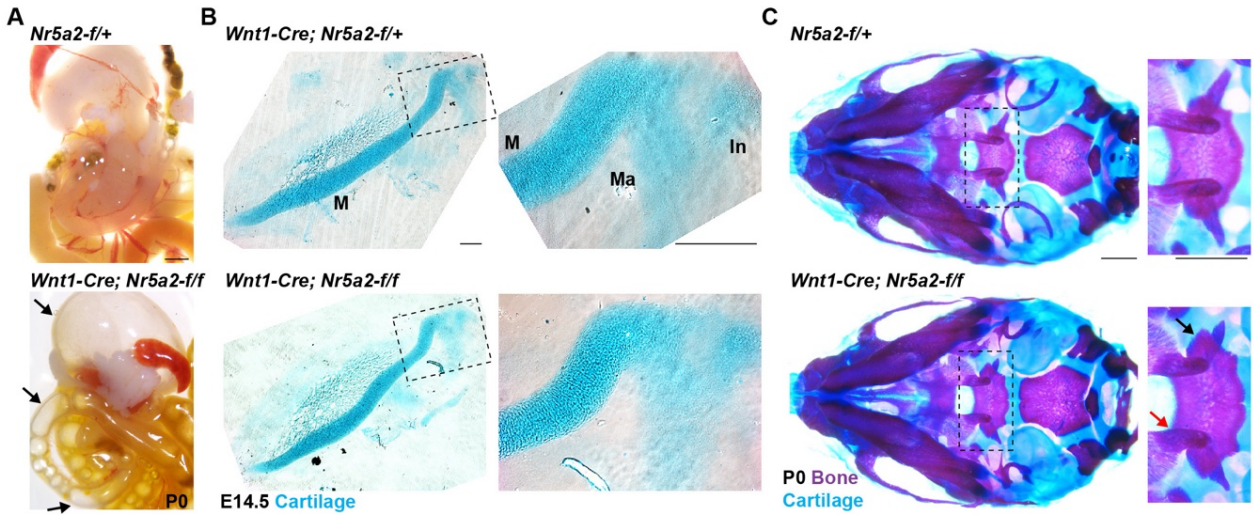


**Figure S4. Detailed phenotypic analysis of mouse conditional *Nr5a2* mutants, related to Figure 4**

(A) Death at birth of *Nr5a2<sup>NCC</sup>* animals (*Wnt1-Cre; Nr5a2-f/f*) correlates with numerous air bubbles (arrows) in their stomach and intestines (freshly dissected). N = 4 each for *Nr5a2<sup>NCC</sup>* mutants and wild types (*Nr5a2-f/+*, *Nr5a2-f/f* or *Wnt1-Cre; Nr5a2-f/+*).

(B) Flat-mount dissections of E14.5 Meckel's cartilages (M, Alcian Blue staining) show no difference in 4/4 *Nr5a2<sup>NCC</sup>* mutants versus 10 littermate controls. Incus (In), malleus (Ma).

(C) Alcian Blue (cartilage) and Alizarin Red (bone) staining of newborns show that, in the pterygoid plate of the cranial base, the lateral edges are enlarged (black arrow) and the medial ridges are shorter (red arrow) in 6/6 *Nr5a2<sup>NCC</sup>* mutants versus 12 littermate controls.

(D) Whole-mount fluorescent images of bone (Alizarin Red, pseudo-colored green) and facial tendons and ligaments (*Scx-GFP+*, pseudo-colored magenta) show dysmorphic lateral jaw tendons (arrows) associated with mandibular bone (Mand) in 4/4 *Nr5a2<sup>NCC</sup>* mutants versus 3 littermate controls. Dashed lines indicate locations of coronal sections in (E).

(E) Coronal sections of the proximal lower jaw at E16.5 reveal dysmorphic muscle fibers (MF20+, green, arrows) in the lower jaw of *Nr5a2<sup>NCC</sup>* mutants versus *Nr5a2-f/+* controls. Tendons are labeled by *Scx-GFP* (magenta) and chondrocytes by anti-Sox9 staining (blue). Similar staining was seen in multiple sections. Angular process (Ang), condyle process (Con).

(F) Measurements of facial skeleton and tendon parameters for the indicated genotypes at P0. Significance was calculated with a Tukey's range test. Error bars represent standard error of the mean. Nonsignificant *p* values (*p* > 0.05) are not shown.

(G) Newborn forelimb and hindlimb skeletons stained with Alcian Blue (cartilage) and Alizarin Red (bone) are unaffected in 10 *Prrx1-Cre; Nr5a2-f/f* mutant limbs versus 38 sibling controls (*Nr5a2-f/+*, *Nr5a2-f/f*, or *Prrx1-Cre; Nr5a2-f/+*) limbs.

(H) Limb tendons and ligaments (*Scx-GFP*, magenta) and muscles (Phalloidin, white) appear normal in 4/4 *Prrx1-Cre; Nr5a2-f/f* mutant limbs versus 8 control littermates at P3.

(I) Freshly dissected tissue shows absence of the salivary gland (arrows) in *Nr5a2<sup>NCC</sup>* mutants. N = 4 each.

(J) Trichrome staining of coronal sections show that parotid and lacrimal glands (arrowheads) are still present in *Nr5a2<sup>NCC</sup>* mutants. N = 4 each. Scale bars = 200  $\mu$ m (B, E, J), 1 mm in all others.

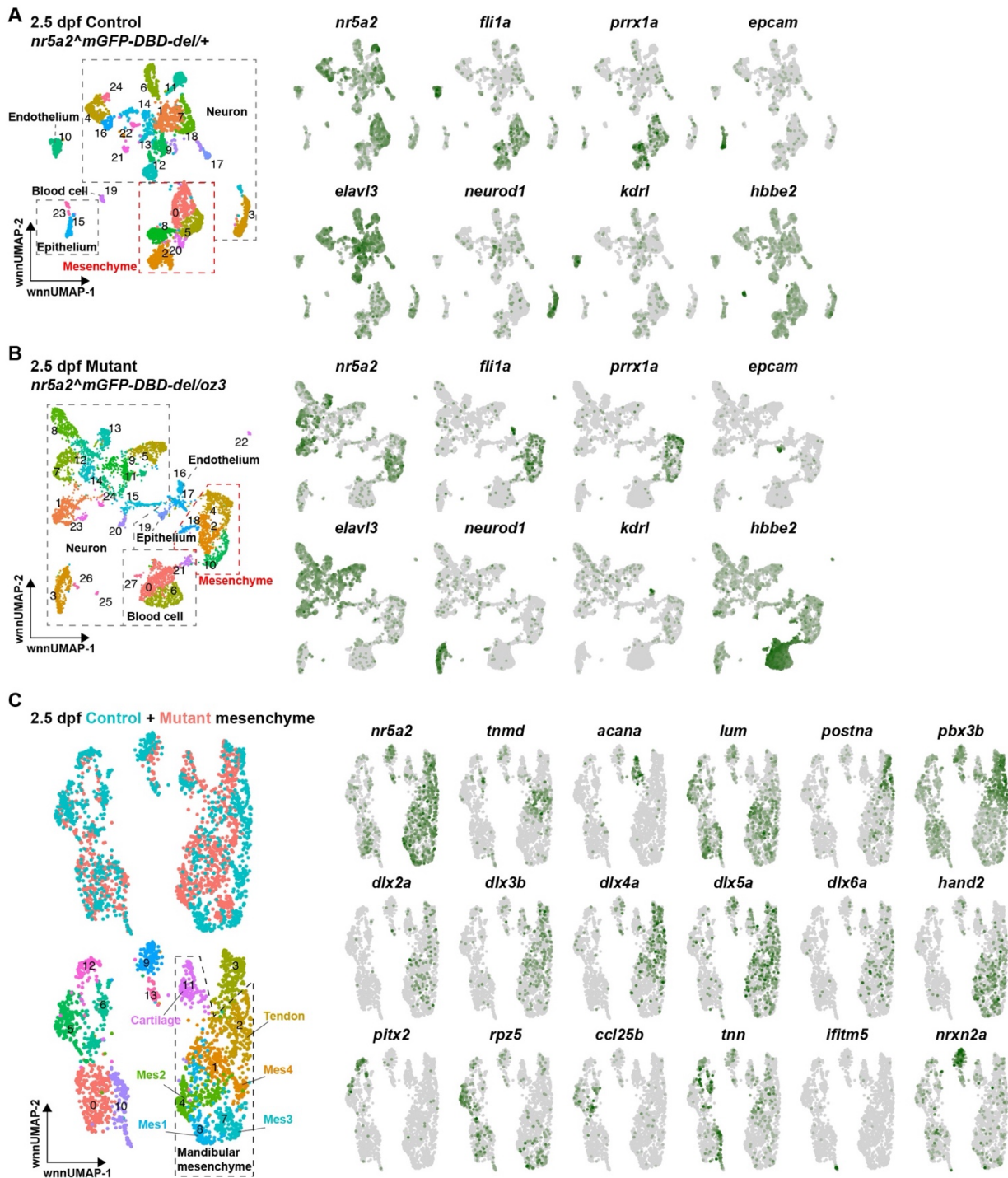


**Figure S5. Single-cell analysis of marker gene expression in entire *nr5a2* mutant and control datasets, related to Figure 5.**

(A, B) Individual UMAPs and clustering of the integrated single-cell chromatin accessibility and transcriptome datasets of control (A, *nr5a2*:mGFP-DBD-del/+) and mutant (B, *nr5a2*:mGFP-DBD-del/oz3). Feature plots show major marker genes used to identify subsets of mesenchyme (*fli1a*<sup>+</sup> and *prrx1a*<sup>+</sup>), epithelium (*epcam*<sup>+</sup>), neurons (*elavl3*<sup>+</sup> or *neurod1*<sup>+</sup>), endothelium (*kdrl*<sup>+</sup>), and blood cells (*hbbe2*<sup>+</sup>).

(C) Re-clustering of mesenchyme (*fli1a*<sup>+</sup> and *prrx1a*<sup>+</sup> in A and B above) from combined control and mutant datasets separated into 14 clusters. Feature plots show major marker genes used to identify the mandibular mesenchyme (*dlx*<sup>+</sup> and *hand2*<sup>+</sup>), tendon (*tnmd*<sup>+</sup>), and cartilage (*acana*<sup>+</sup>) clusters used for detailed analysis.

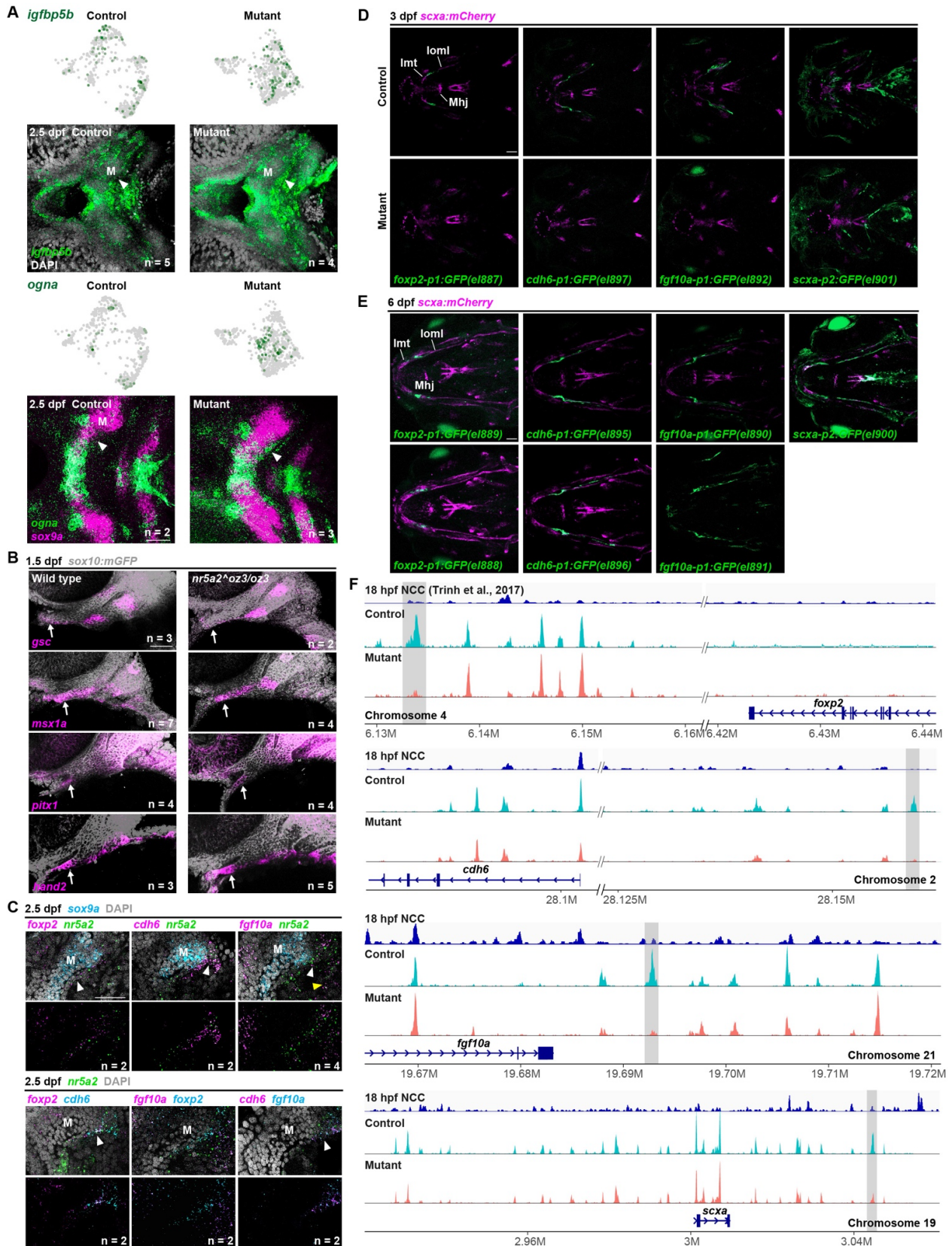


**Figure S6. Analysis of Nr5a2-regulated enhancers, upregulated genes in *nr5a2* mutants, and normal axis patterning in *nr5a2* mutants, related to Figure 6.**

(A) Feature plots show increased *igfbp5b* and *ogna* transcripts in mutant snRNAseq datasets of mandibular mesenchyme. Ventral views of fluorescent in situ hybridizations show increased expression of *igfbp5b* and *ogna* posterior to Meckel's (M) cartilage (arrowheads) in mutants (*nr5a2:mGFP-DBD-del/oz3*) compared to controls (*nr5a2:mGFP-DBD-del/+*). DAPI staining labels all nuclei for *igfbp5b* in situ, and *sox9a* expression highlights Meckel's cartilage for *ogna* in situ.

(B) Lateral facial views of in situ hybridizations show that markers of the aboral (*gsc* and *msx1a*), oral (*pitx1*), and ventral (*hand2*) domains are largely unaffected in *nr5a2* mutants (arrows denote jaw expression domains). Anti-GFP staining for *sox10:mGFP* highlights arch CNCCs in white.

(C) RNAscope in situ hybridizations at 2.5 dpf show Meckel's cartilage and surrounding mesenchyme, with *sox9a* expression labeling chondrocytes in blue (top panels) and DAPI labeling all nuclei in white. Top, white arrowheads denote co-localization of *nr5a2* with *foxp2*, *cdh6*, and *fgf10a* expression within the perichondrium, and yellow arrowhead denotes co-localization of *nr5a2* with midline *fgf10a* expression. Bottom, white arrowheads denote co-localization of *cdh6* with *foxp2* and *fgf10a* in the perichondrium; *fgf10a* and *foxp2* expression are largely non-overlapping.


(D) Earlier transgenic activity at 3 dpf for the same individuals shown in Figure 6. *foxp2-p1*, *cdh6-p1*, and *fgf10a-p1* lines display GFP expression posterior to Meckel's cartilage, yet only few *scxa-p2:GFP+* cells are seen at this stage. For each transgenic line, GFP expression was absent in *nr5a2<sup>oz3/oz3</sup>* mutants. Tendons and ligaments are labeled by *scxa:mCherry* in magenta. Intermandibular tendon (Imt), interopercular-mandibular ligament (Ioml), mandibulohyoid junction tendon (Mhj).

(E) Independently isolated transgenic lines for each enhancer tested in Figure 6 show consistent GFP expression posterior to Meckel's cartilage. Scale bars = 50  $\mu$ m.

(F) Genome views of the *foxp2*, *cdh6*, *fgf10a*, and *scxa* loci for the snATACseq datasets of controls and mutants at 2.5 dpf show the highly specific reduction of chromatin accessibility in the regions highlighted in grey (tested in D and E). Tested enhancer regions had little to no accessibility in migratory CNCCs at 18 hours post-fertilization (hpf) [S4]. Note that the 18 hpf ATACseq tracks and the snATACseq tracks are not at the same scale. Omitted regions display minimal accessibility.

## Supplemental References

- S1. Yuan, Y., Loh, Y.E., Han, X., Feng, J., Ho, T.V., He, J., Jing, J., Groff, K., Wu, A., and Chai, Y. (2020). Spatiotemporal cellular movement and fate decisions during first pharyngeal arch morphogenesis. *Sci Adv* 6. 10.1126/sciadv.abb0119.
- S2. Visel, A., Thaller, C., and Eichele, G. (2004). GenePaint.org: an atlas of gene expression patterns in the mouse embryo. *Nucleic Acids Res* 32, D552-556. 10.1093/nar/gkh029.
- S3. Hauser, B.R., Aure, M.H., Kelly, M.C., Hoffman, M.P., Chibly, A.M., and Core, G.a.C.B. (2020). Generation of a Single-Cell RNAseq Atlas of Murine Salivary Gland Development. *iScience* 23, 101838. 10.1016/j.isci.2020.101838.
- S4. Trinh, L.A., Chong-Morrison, V., Gavriouchkina, D., Hochgreb-Hagele, T., Senanayake, U., Fraser, S.E., and Sauka-Spengler, T. (2017). Biotagging of Specific Cell Populations in Zebrafish Reveals Gene Regulatory Logic Encoded in the Nuclear Transcriptome. *Cell Rep* 19, 425-440. 10.1016/j.celrep.2017.03.045.



[Click here to access/download](#)

**Supplemental Videos and Spreadsheets**  
**Table S1.xlsx**







[Click here to access/download](#)

**Supplemental Videos and Spreadsheets**

**Table S2.xlsx**






[Click here to access/download](#)

**Supplemental Videos and Spreadsheets**

**Table S3.xlsx**





[Click here to access/download](#)

**Supplemental Videos and Spreadsheets**  
**Table S4.xlsx**





[Click here to access/download](#)

**Supplemental Videos and Spreadsheets**

**Table S5.xlsx**





[Click here to access/download](#)

**Supplemental Videos and Spreadsheets**

**Table S6.xlsx**

